UNIVERSITY OF OKLAHOMA

GRADUATE COLLEGE

INVESTIGATION OF A FREQUENCY AND PATTERN RECONFIGURABLE SLOT ARRAY UTILIZING RING RESONATOR END LOADS

A THESIS

SUBMITTED TO THE GRADUATE FACULTY

in partial fulfillment of the requirements for the

Degree of

MASTER OF SCIENCE

By

STEPHEN BASS

Norman, Oklahoma

2017

INVESTIGATION OF A FREQUENCY AND PATTERN RECONFIGURABLE SLOT ARRAY UTILIZING RING RESONATOR END LOADS

A THESIS APPROVED FOR THE
SCHOOL OF ELECTRICAL AND COMPUTER ENGINEERING

BY

Dr. Jessica Ruyle, Chair

Dr. Caleb Fulton

Dr. Hjalti Sigmarsson

Table of Contents

List of Tables vi

List of Figures vii

Abstract xii

1 Introduction 1

2 Slot Antenna Theory 6
- 2.1 Transmission Line Model . . . 7
  - 2.1.1 Input Impedance . . . 7
  - 2.1.2 Voltage Distribution . . . 11
- 2.2 Radiation Pattern . . . 15
  - 2.2.1 Near Field due to the Slot Aperture . . . 15
  - 2.2.2 Far Fields over an Infinite Ground Plane . . . 17
  - 2.2.3 Far Fields over a Finite Ground Plane . . . 19
- 2.3 Conclusions . . . 22

3 Ring Resonator End Loaded Slot Antenna (RRELSA) 24
- 3.1 Original Design . . . 24
- 3.2 Theory of Design . . . 25
- 3.3 End Load Design . . . 28
- 3.4 Bias Line . . . 31
  - 3.4.1 Microstrip Bias Line . . . 31
  - 3.4.2 Coplanar Waveguide Bias Line . . . 32
- 3.5 Feeding Network . . . 33
- 3.6 Conclusions . . . 36

4 Linear Yagi-Uda Style Arrays 37
- 4.1 Element Design . . . 37
- 4.2 Coupling . . . 40
  - 4.2.1 Transmission Line Even/Odd Mode Coupling . . . 40
  - 4.2.2 Radiative Coupling . . . 42
- 4.3 Input Impedance . . . 46

4.4 Radiation Pattern 50
4.5 Conclusions 61

5 RRELSA Array **63**
5.1 Basic Design 63
5.1.1 Element Tuning 64
5.1.2 Spacing 66
5.1.3 Ground Plane 67
5.1.4 Bent Microstrip Feed 67
5.2 Final Designs and Results 70
5.2.1 Original Design 70
5.2.2 New Design at 2 GHz 72
5.2.3 New Design at 4 GHz 76
5.3 Conclusions 83

6 Conclusions and Future Work **84**
6.1 Conclusions 84
6.2 Scientific Impact 85
6.3 Future Work 85

References **87**

List of Tables

5.1 Tabulated measurement results from the three designs, specifically gain, percent reconfigurable bandwidth, and the maximum beam tilt achieved for each design. A range of measured gain is given because the arrays are pattern reconfigurable and it can change based on the configuration. 83

List of Figures

1.1 Phased array showing pattern reconfigurability. Each element can be phase shifted so that the total electric field can be steered in a specific direction. 3
1.2 Original design of the RRELSA from [2] (a) and the reflection coefficient (b) showing frequency reconfigurability. 4
1.3 Traditional Yagi-Uda antenna (a) and the Yagi-Uda variation proposed in this work (b). Both antennas achieve directionality with parasitic antennas, but the variation proposed here is reconfigurable. 5

2.1 Slot antenna modeled as a lossy transmission line. The end loads, Z_L, can be replaced by short circuits for a standard slot antenna. . . 7
2.2 Normalized voltage distributions calculated for (a) half- and (b) full-wavelength slots loaded with ideal shorts. 15
2.3 Directivity (in dB) of a half-wavelength slot on an infinite ground plane. 18
2.4 Diffracted fields at edge point Q from source point s on an edge along the $\hat{\mathbf{v}}$ axis. 20
2.5 Directivity (in dB) of a half-wavelength slot lying in the x-y plane on a finite ground plane. UTD method (blue solid line) compared to HFSS results (red dotted line). 21
2.6 Directivity (in dB) in the E-plane of a half-wavelength slot lying off-center in the x-y plane on a finite, square ground plane that has a side length of λ. The calculated radiation pattern using UTD (blue line) is compared to an HFSS simulation (red line). The slot is shifted in the x direction by (a,b) -λ/4, (c,d) λ/4, and (e,f) 0, for comparison 23

3.1 (a) Reflection coefficient, (b) peak gain, and (c) cross polarized gain of the Ring Resonator End Loaded Slot Antenna across frequency for different voltage biasing [2]. 26

3.2 Initial design of the Ring Resonator End Loaded Slot Antenna [2]. Shown is (a) graphic model, (b) the front and (c) the back of the fabricated antenna along with the mounting device used during measurement. The RRELSA is connected to the AC generator with a bias tee to prevent DC power from flowing back to the AC generator. 27
3.3 Physical (a), matrix (b), and circuit (c) model of the slot ring resonator loads implemented at the ends of the RRELSA. The ring resonator can be modeled as a slotline split into three lengths, l_1, l_2, and l_3, by the varactors. By cascading the three transmission lines and two varactors using ABCD parameters (b) and using an equivalent pi-network (c), the input impedance can be calculated. . . 29
3.4 Redesigned slot ring resonator featuring a taper to improve the accuracy of the model. The wide aperture of the main radiating slot aperture, w_a, is tapered down to a small input port over a length of l_{taper} to better model the ring resonator. 30
3.5 S-Parameters and picture of the fabricated bandstop filter. 33
3.6 Microstrip feed (dotted line) underneath a slot antenna (solid line). (a) straight stub, (b) radial stub 34
3.7 Model of the microstrip-coupled slot antenna(a) with a transformer and (b using an equivalent series impedance of the slot antenna, Z_{sL}. 35
3.8 Impedance seen at the microstrip feed line, Z_{sL}, due to the RRELSA tuned to different frequencies. Circuit model method (blue solid line) compared to HFSS results (red dotted line). 36

4.1 Design table for Yagi-Uda antennas from [19] 38
4.2 Design table for Yagi-Uda antennas from [19] 39
4.3 Diagram depicting how the impedance matrix will be used. Two matrices will be cascaded with the center transmission line being fed and the ends of the lines having reconfigurable loads. 41
4.4 Adjacent dipoles (a) and slot antennas (b) that couple into each other with far-field radiation. 44
4.5 Multiport network reduced by loading k ports with load impedances [32]. 47
4.6 Yagi-Uda array of three linear dipoles spaced d apart along the x-axis. The x-z cut is shown in (a) and the x-y cut is shown in (b). . . 49
4.7 H-plane cut of the array factor and radiation pattern of a Yagi-Uda style dipole array. Directivity increases as the left and right dipoles become electrically larger and smaller than the fed element. 56
4.8 E-plane cut of the array factor and radiation pattern of a Yagi-Uda style slot array. Directivity increases as the left and right dipoles become electrically larger and smaller than the fed element. 57

4.9 E-plane cut of the radiation pattern of a Yagi-Uda style slot array. (a) uses array factor assuming each element radiation pattern is the same, (b) takes the different radiation patterns into account. 59
4.10 Linear Yagi-Uda slot antenna array truncated so that each element is the same electrical size. The end loads enable each to have a different effective size to maintain the directionality of the Yagi-Uda array. 60
4.11 Radiation patterns of a slot antenna array loaded with ideal inductors to create an effective Yagi-Uda array. Each slot element is physically the same size, but the loads give each element an effective electrical length that can direct the radiation pattern like a Yagi-Uda antenna. 61

5.1 Design of the RRELSA Array. Three elements are placed next to each other in a Yagi-Uda configuration to achieve directionality. By tuning the outer elements, the radiation pattern can be bent from broadside. 64
5.2 Definitions of three dimensions of the RRELSA array discussed in this chapter. The element spacing is defined from the center of each element, and the ground width and length are different dimensions of the ground plane. 65
5.3 Analysis on the electrical size of the ground plane. The design was initialized with an element spacing of 37.5 mm, a ground width of 1.5λ, and a ground length of 2.0λ. Each dimensions was then varied individually from this design. 68
5.4 Tapered slot with a (a) straight feed as implemented in the original RRELSA design [2], and (b) a bent feed and radial tuning stub to be implemented in the array. Also shown are the bias lines that connect to the ring resonator loads. 69
5.5 Fabricated RRELSA array using the original design of the RRELSA from Szolc [2]. Bias lines can be seen along the edge of the ground plane to minimize their interference with the radiation pattern. . . . 71
5.6 Measured reflection coefficient for the RRELSA array using the original design of the RRELSA in [2]. 71
5.7 Directivity (a), realized gain (b), real (c) and imaginary (d) impedance, and the reflection coefficient (e) for the RRELSA array using the original element from [2] and tuned to 1.85 GHz. Measured values (blue) are compared to the circuit model described in this thesis (red) and an HFSS simulation (yellow). 73

5.8 Directivity (a), realized gain (b), real (c) and imaginary (d) impedance, and the reflection coefficient (e) for the RRELSA array using the original element from [2] and tuned to 2.0 GHz. Measured values (blue) are compared to the circuit model described in this thesis (red) and an HFSS simulation (yellow). 74
5.9 Fabricated RRELSA array using a new design of the RRELSA. The new design primarily differs from the original by the tapered loads (a), and the microstrip feed line that is connected to the ground plane with a via (b). 75
5.10 Measured reflection coefficient for the RRELSA array using a new design, as described in this thesis. 76
5.11 Directivity (a), realized gain (b), real (c) and imaginary (d) impedance, and the reflection coefficient (e) for the redesigned RRELSA array centered and tuned to 2.0 GHz. Measured values (blue) are compared to the circuit model described in this thesis (red) and an HFSS simulation (yellow). 77
5.12 Directivity (a), realized gain (b), real (c) and imaginary (d) impedance, and the reflection coefficient (e) for the redesigned RRELSA array centered at 2 GHz and tuned to 2.3 GHz. Measured values (blue) are compared to the circuit model described in this thesis (red) and an HFSS simulation (yellow). 78
5.13 Fabricated RRELSA array using a new design of the RRELSA. This array has about a quarter the surface area of the other designs. . . . 79
5.14 Measured reflection coefficient for the RRELSA array using the new array and designed at 4 GHz. 80
5.15 Directivity (a), realized gain (b), real (c) and imaginary (d) impedance, and the reflection coefficient (e) for the redesigned RRELSA array centered at 4 GHz and tuned to 3 GHz. Measured values (blue) are compared to the circuit model described in this thesis (red) and an HFSS simulation (yellow). 81
5.16 Directivity (a), realized gain (b), real (c) and imaginary (d) impedance, and the reflection coefficient (e) for the redesigned RRELSA array centered and tuned to 4 GHz. Measured values (blue) are compared to the circuit model described in this thesis (red) and an HFSS simulation (yellow). 82

Abstract

Fixed-bandwidth wireless systems are forced to operate in preallocated blocks of frequencies, often wasting valuable spectrum. Whereas, systems with reconfigurable antennas that can tune resonant frequency, polarization, or pattern allow for versatile systems and efficient spectrum use. Reconfigurable antennas have largely been designed using microstrip transmission line structures since they can be easily printed on a dielectric substrate, making the antenna compact, inexpensive to fabricate, and simple to integrate active components in a series configuration. Slotline is similarly easy to fabricate and has been shown to have some advantages over microstrip in applications such as when active components in a shunt configuration are desired. However, not many reconfigurable antenna architectures have been developed in slotline. Additionally, while frequency- and polarization-agile antennas have been reported by many researchers, antennas with both frequency and pattern reconfiguration capabilities are significantly rare.

In this thesis, a closed-form analytical solution for a Yagi-Uda array of loaded slot antennas will be presented. This analysis first evaluates each slot antenna using an established transmission line model then calculates the coupling between the elements using the relative induced power on each antenna. Network parameters are then utilized to model the effects the slot antennas have on each other. The Induced EMF method uses the power incident on one antenna due to another to find the mutual impedance between them - allowing the presented method to be gener-

alizable to any Yagi-Uda array of elements where the radiation pattern is known. The network parameters will be shown to provide an array factor for the Yagi-Uda array - predicting the radiative and directive properties of the array in a closed-form analysis. The analysis method will also be shown to predict the input impedance of the driven element of the array, including the impact of mutual coupling from the parasitic elements, across frequency and for arbitrary array spacings - a result that has not been available with previous analysis methods.

Chapter 1

Introduction

Basic antenna systems with fixed bandwidths need allocated blocks of frequencies so that different systems can operate at their designed frequency without interfering with another source. Alternatively, reconfigurable antennas have the ability to alter their radiating properties, allowing a more fluid approach to bandwidth allocation [1], [2]. This approach would have the antennas switch to an available frequency when it is needed instead of having certain frequencies restricted to certain systems even when not in use, allowing the available spectrum to be used more efficiently. Some reconfigurable antennas have been designed with mechanical switches or moving parts for reconfiguration. However the reconfiguration process for these systems can be slow and cause the parts to wear out, so efforts have been made to design reconfigurable antennas that can be switched electronically allowing for a smoother and faster reconfiguration.

In addition to the operating frequency, another property that can be reconfigured is the radiation pattern of the antenna [3]. A straightforward solution would be to physically move or rotate the antenna to shift where the primary radiating beam points. However, this method tends to be slow and the addition of motors and moving parts that can break down decreases its reliability [3]. By electrically reconfiguring the radiation pattern instead, the antenna would reconfigure faster and be

more durable over time. One commonly-used solution is to place many antennas in a phased array using phase shifters to steer the beam [4], [5], shown in Figure 1.1. While effective, phased arrays must feed multiple elements with phase-shifted signals to operate, which significantly increases the complexity of the system [4], [5]. Another solution to pattern reconfigurability is to use a Yagi-Uda based design, shown in Figure 1.3.a [6]–[9]. The Yagi-Uda antenna array is one of the oldest directive antenna designs. The main advantage of a Yagi-Uda design is the achievement of a directive radiation pattern purely through parasitic coupling to nearby passive elements [6]. The mutual coupling behavior that drives the performance of the array is element dependent, so while the basic Yagi-Uda antenna array is static and is only directive in one direction, if each element in the array were reconfigurable, it would be possible to change the direction of radiation. Previous work has pursued a closed-form analysis of the Yagi-Uda array performance through mutual impedance/admittance; however, it was limited to dipole antennas [10], [11]. Classic Yagi-Uda antennas are simple dipole arrays with lengths and spacings designed using well-established tables that allow a designer to electrically scale the array to a desired operating frequency. Other elements besides dipoles can also be used to create a directive Yagi-Uda array; however, the design process for an array with other elements is not well established. Non-dipole Yagi-Uda antenna arrays are typically designed using the dipole tables and then tuned using a full wave computational electromagnetic solver to achieve the desired performance. A generalized, closed-form, analytical solution to the design of a Yagi-Uda antenna array, as shown in this thesis, would eliminate the need of the Yagi-Uda design tables while also providing a deeper understanding to the structure and allowing the use of reconfigurable elements. In order to design an array with both frequency and pattern reconfigurability, it is necessary to choose an element that is easily reconfigurable.

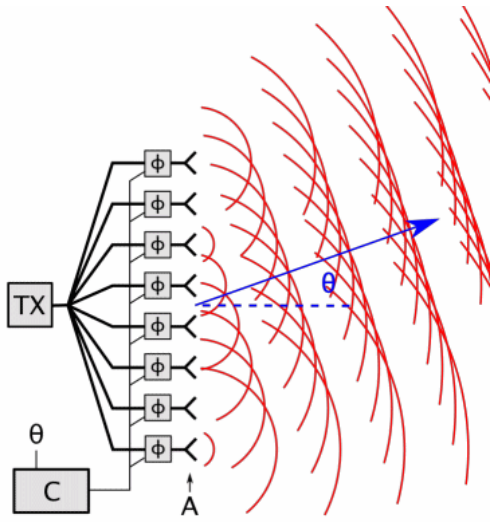

Figure 1.1: Phased array showing pattern reconfigurability. Each element can be phase shifted so that the total electric field can be steered in a specific direction.

Many reconfigurable antennas have been designed using microstrip transmission line structures since they can be easily printed on a dielectric substrate, making the antenna compact and inexpensive to fabricate and simple to integrate active components in a series configuration [12]. Slotline is similarly easy to fabricate and has been shown to have advantages over microstrip in some applications such as when active components in a shunt configuration or a bi-directional radiation pattern is desired [2], [13]. However, not many reconfigurable antenna architectures have been developed in slotline. One such antenna, the Ring Resonator End Loaded Slot Antenna (RRELSA), achieves frequency reconfigurability by implementing tunable end loads in shunt configuration [2]. While a simple slot antenna is shorted on the end, this slot antenna is loaded with ring resonators and tunable varactors to change the effective impedance seen at the end, thereby changing the resonant frequency as well. Using this configuration, it has been shown that the RRELSA can be continuously tuned from 1.65 to 2.9 GHz [2], shown in Figure 1.2. By using this element in a Yagi-Uda array, both pattern and frequency reconfiguration can be

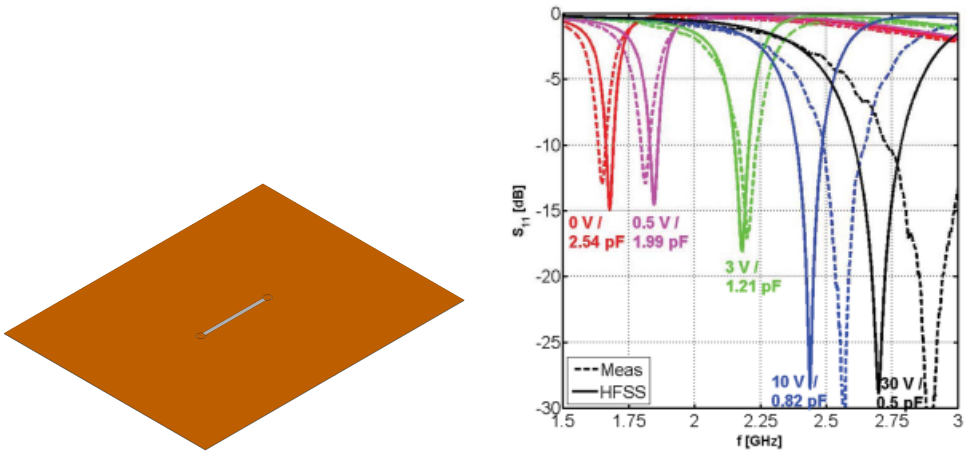

(a) (b)

Figure 1.2: Original design of the RRELSA from [2] (a) and the reflection coefficient (b) showing frequency reconfigurability.

achieved.

In this thesis, the RRELSA is implemented in a Yagi-Uda style array, shown in Figure 1.3.b, in order to obtain continuous reconfigurability in both frequency and radiation pattern, simultaneously. Additionally, an analytical model of the array is derived to allow for quickly designing a similar array for a different frequency range or substrate configuration.

This thesis begins with an overview of the transmission line model of a slot antenna in Chapter 2. This model allows the use of an arbitrary end load, enabling the use of the ring resonator of the RRELSA and is able to determine the radiation pattern and input impedance of the slot antenna. Chapter 3 introduces the initial design of the RRELSA and discusses a few improvements to the design and how it could be modified to change its frequency reconfigurable range. In Chapter 4, the linear Yagi-Uda style arrays are analyzed and a couple of methods to calculate the mutual impedance/admittance between the elements are discussed. Additionally, this chapter derives how to determine the total radiated fields of a linear array using array

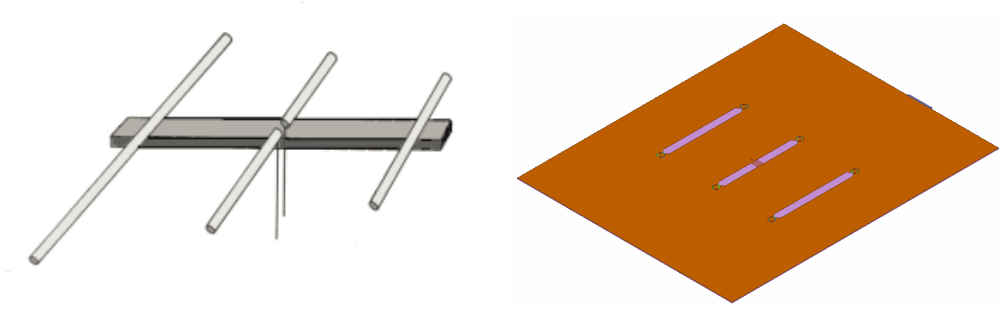

(a) (b)

Figure 1.3: Traditional Yagi-Uda antenna (a) and the Yagi-Uda variation proposed in this work (b). Both antennas achieve directionality with parasitic antennas, but the variation proposed here is reconfigurable.

factor theory. The completed RRELSA Array is designed in Chapter 5 following the methods discussed in the previous chapters. Simulated results and measurements from fabricated antennas are also shown and the input impedance and radiation patterns are compared. Finally, this thesis concludes in Chapter 6 with an analysis of the completed work and recommendations for continuing research on this topic.

Chapter 2

Slot Antenna Theory

The standard slot antenna is simply a slotline that is terminated on both ends with a short circuit and fed with a voltage source across its width. This can be easily fabricated by removing a rectangular section from a copper ground plane. More complex slot antennas can have end loads other than a short circuit which can be used to make the slot reconfigurable [2]. In order to fully characterize the end-loaded slot design discussed later in this thesis, it is necessary to develop a model that can account for arbitrary end-loads. Instead of using a full wave computational electromagnetics solver to model the slot antenna, an analytical model of the structure was developed to aid the design process. The model used includes transmission line theory to calculate the input impedance and the voltage distribution across the slot as well as the Uniform Theory of Wedge Diffraction to account for the radiation effects of the finite ground plane edges. By utilizing this model for the loaded slot antennas in the array, each element can be independently characterized to better account for their interactions.

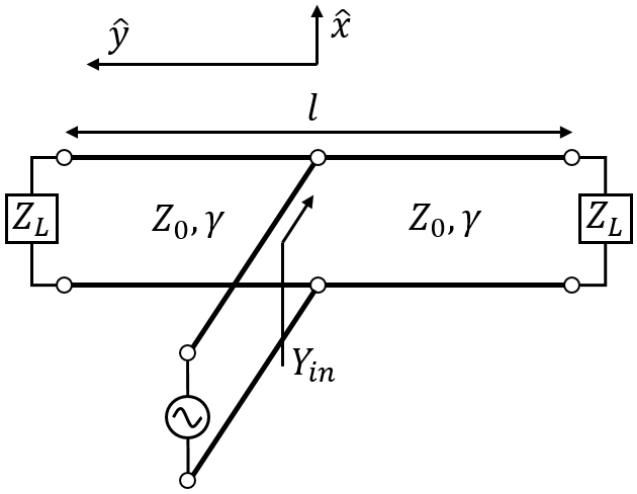

Figure 2.1: Slot antenna modeled as a lossy transmission line. The end loads, Z_L, can be replaced by short circuits for a standard slot antenna.

2.1 Transmission Line Model

A radiating slot antenna can be modeled as a lossy, loaded transmission line [13], [14], as shown in Figure 2.1. For a simple slot, the end loads on the transmission line structure are replaced with short circuits, but it is important to keep the arbitrary loads to enable characterization of a non-standard slot antenna. In order to expand a single slot antenna into an array, two of the most important parameters to characterize are the input impedance and the voltage distribution along the length of the slot.

2.1.1 Input Impedance

In order to calculate the input impedance of a slot antenna, it has been shown in [13] that it is first necessary to calculate the characteristic impedance, Z_0, and the propagation constant, γ of the radiating slot line. Both equations can be found using

transmission line theory [15] and the equations

$$Z_0 = \sqrt{\frac{R_c + j\omega L_c}{G_c + j\omega C_c}} \tag{2.1}$$

and

$$\gamma = \sqrt{(R_c + j\omega L_c)(G_c + j\omega C_c)} \tag{2.2}$$

where R_c, G_c, L_c, and C_c are the lossy-line per-unit-length transmission parameters resistance, conductance, inductance, and capacitance, respectively, and ω is the radian frequency [15]. The per-unit-length parameters of the slot can be calculated using the perturbational theory so that the inductance and capacitance per-unit-length can be analyzed for the lossless case, then the resistance and conductance per-unit-length can be added afterward. The inductance and capacitance per-unit-length can be calculated using the lossless transmission line equations

$$\frac{\omega}{\beta} = \frac{1}{\sqrt{L_c C_c}} \tag{2.3}$$

and

$$Z_0^{lossless} = \sqrt{\frac{L_c}{C_c}} \tag{2.4}$$

from [15] which can be used to solve for the inductance and capacitance per-unit-length such that

$$L_c = \frac{\beta}{\omega} Z_0^{lossless} \tag{2.5}$$

and

$$C_c = \frac{\beta}{\omega} \frac{1}{Z_0^{lossless}} \tag{2.6}$$

where the phase constant, β, and the lossless characteristic impedance, $Z_0^{lossless}$, are calculated using Cohn's method [16].

The resistance per-unit-length can be obtained using an approximation from twin lead transmission line, as shown in [13]. The resistance of the metal around the slot and in the twin lean wires is

$$R_s = \frac{1}{\delta_s \sigma} = \sqrt{\frac{\omega\mu}{2\sigma}} \tag{2.7}$$

where δ_s is the skin depth, and σ and μ are the conductivity and permeability of the metal. For twin lead, the resistance per-unit-length equation would then be

$$R_c = \frac{R_s}{\pi a} \tag{2.8}$$

where a is the radius of the wire. For a slot, an effective radius can be used [13] as

$$a = \frac{w + h_m}{40} \left(\frac{\lambda}{\lambda_0} \right)^2 \tag{2.9}$$

where w is the width of the slot, h_m is the height of the metal, λ_0 is the free-space wavelength, and λ is the effective wavelength defined by Cohn's method [16]. The conductance per-unit-length is a loss factor primarily made up of two parts: loss due to imperfections in the dielectric substrate, G_{loss}, and loss due to radiation, G_r. The dielectric loss parameter can be approximated using a parallel plate waveguide model [13] so that

$$G_{loss} = 2\pi f \delta \epsilon_0 \left(\frac{\lambda_0}{\lambda} \right)^2 4\frac{h_m}{w} \tag{2.10}$$

where $\tan(\delta)$ is the dielectric loss tangent of the substrate. The radiation conduc-

tance can be calculated using

$$P_r = \int_{-\frac{l}{2}}^{\frac{l}{2}} \frac{1}{2}|V(y)|^2 G_r dy \tag{2.11}$$

where $V(y)$ is the voltage distribution across the slot as derived in Section 2.1.2 of this thesis, l is the length of the slot, and P_r is the power radiated by the slot as found in [13].

Once Z_0 and γ are calculated, the input impedance looking into each end of a center-fed, loaded slot is [15]

$$Z_{in,left} = Z_0 \frac{Z_{L,left} + Z_0 \tanh(\gamma \frac{l}{2})}{Z_0 + Z_{L,left} \tanh(\gamma \frac{l}{2})} \tag{2.12}$$

$$Z_{in,right} = Z_0 \frac{Z_{L,right} + Z_0 \tanh(\gamma \frac{l}{2})}{Z_0 + Z_{L,right} \tanh(\gamma \frac{l}{2})} \tag{2.13}$$

where $Z_{in,left}$ and $Z_{in,right}$ are the input impedances looking into the left and right sides and $Z_{L,left}$ and $Z_{L,right}$ are the left and right end load impedances, respectively. The ends of a slot antenna are in parallel. So the input impedance seen at the driven port is

$$Z_{in} = \frac{Z_{in,left} Z_{in,right}}{Z_{in,left} + Z_{in,right}} \tag{2.14}$$

if the each end is loaded differently. If each load is the same, the equations reduce to

$$Z_{in,half} = Z_{in,left} = Z_{in,right} \tag{2.15}$$

$$Z_{in} = \frac{1}{2} Z_{in,half}. \tag{2.16}$$

In either case, if the input admittance to the slot antenna is also needed, it can be

found by taking the inverse of the input impedance, as in

$$Y_{in} = \frac{1}{Z_{in}}. \tag{2.17}$$

This method of calculating the input impedance was shown to be accurate based on simulation and fabricated results in [13].

2.1.2 Voltage Distribution

According to transmission line theory, the voltage and current distributions on a transmission line in the lossless case can be defined using the solutions to Helmholtz equations [17]:

$$\nabla^2 E(x, y, z) + \beta^2 E(x, y, z) = 0 \tag{2.18}$$

where E is the electric field on the line, β is the propagation constant of the media, and y is the position similarly defined as in Figure 2.1. Solutions to this equation can be used to derive the form of the voltage distribution across a transmission line using modal analysis. Typically for transmission lines, the solution to this equation takes the form

$$f(y) = Ae^{-j\beta y} + Be^{+j\beta y} \tag{2.19}$$

where A and B are constants determined by the boundary conditions of the line [17]. This equation takes into account the forward and backward traveling waves on the line. However, for a resonator with a standing wave, a different solution is more appropriate [17]. The new solution,

$$g(y) = C\cos(\beta y) + D\sin(\beta y) \tag{2.20}$$

better takes into account the standing waves on a transmission line resonator. Because voltage and electric field are closely related assuming transverse electric and magnetic field modes, the standing wave voltage distribution on a lossless transmission line resonator, such as the one shown in Figure 2.1, can be defined as

$$V(y) = V_0(C\cos(\beta y) + D\sin(\beta y)) \tag{2.21}$$

where V_0 is the excitation voltage, z is the distance from the center of the slot, β is the phase constant of the line, and C and D are constants [17]. Similarly, the current distribution and impedance across the slot is

$$I(y) = \frac{V_0}{Z_0}(Ccos(\beta y - \frac{\pi}{2}) + Dsin(\beta y - \frac{\pi}{2})) = \frac{V_0}{Z_0}(Csin(\beta y) - Dcos(\beta y)) \tag{2.22}$$

and

$$Z(y) = \frac{V(y)}{I(y)} = Z_0\frac{Ccos(\beta y) + Dsin(\beta z)}{Csin(\beta y) - Dcos(\beta y)} = Z_0\frac{cos(\beta y) + \frac{D}{C}sin(\beta y)}{sin(\beta y) - \frac{D}{C}cos(\beta y)}. \tag{2.23}$$

In order to find the voltage distribution along the length of the slot antenna, boundary conditions can be used at the ends of the slot antenna to find values for the constants, C and D. For an arbitrary slot of length l, the impedance at $\frac{l}{2}$ and $-\frac{l}{2}$ is equal to the impedance of the end loads. For a simple slot, this is simply the impedance of the shorted ends. Then we have that

$$Z(l/2) = Z_0\frac{cos(\beta\frac{l}{2}) + \frac{D}{C}sin(\beta\frac{l}{2})}{sin(\beta\frac{l}{2}) - \frac{D}{C}cos(\beta\frac{l}{2})} = Z_L \tag{2.24}$$

and

$$Z(-l/2) = Z_0\frac{cos(\beta\frac{l}{2}) - \frac{D}{C}sin(\beta\frac{l}{2})}{-sin(\beta\frac{l}{2}) - \frac{D}{C}cos(\beta\frac{l}{2})} = Z_L. \tag{2.25}$$

Assuming the loads at each end of the slot are the same, Equations 2.24 and 2.25 can be combined into one expression. This results in an expression for valid values of β that signify the different modes supported on the slot:

$$\beta_m = \frac{m\pi}{l} \tag{2.26}$$

where m is an integer and the number of the mode. This implies that there are an infinite number of modes that exist in the voltage distribution, each with a different significance based on the structure of the antenna and the frequency. In order to account for all of the modes possible, they must be included in a summation with their modal weights, A_m, which determines the primary modes in the distribution. From Equations 2.21 and 2.26, a modal form of the voltage distribution across the slot can be determined as

$$V(y) = V_0 C \sum_{m=1}^{\infty} A_m (cos(\beta_m y) + \frac{D}{C} sin(\beta_m y)) \tag{2.27}$$

where $\frac{D}{C}$ is defined later in Equation 2.31 and the modal weight can be approximated as

$$A_m = \frac{1}{1 - |\beta_m - \beta|^2}. \tag{2.28}$$

This form of the modal weight ensures that the modes are weighted based on the how similar the modal phase constant is to the generator driven phase constant [13]. The magnitude of the voltage distribution is composed of the constants V_0 and C. The voltage seen at the feed point, V_0 can be defined as

$$V_0 = \frac{Z_{in}}{Z_{in} + Z_0} \tag{2.29}$$

and C is a normalization factor that takes into account the location of the generator, as in

$$C = \frac{1}{\sum_{m=1}^{\infty} A_m(cos(\beta_m y_g) + \frac{D}{C} sin(\beta y_g))} \tag{2.30}$$

where y_g is the position of the generator along the slot.

Similarly, by solving Equation 2.24 using modal analysis, an expression can be found for $\frac{D}{C}$, which is dependent on the load impedance, Z_L, the characteristic impedance of the line, Z_0, the modal propagation constant, β_m, and the length of the slot, l:

$$\frac{D}{C} = \frac{Z_L sin(\beta_m \frac{l}{2}) - Z_0 cos(\beta_m \frac{l}{2})}{Z_L cos(\beta_m \frac{l}{2}) + Z_0 sin(\beta_m \frac{l}{2})}. \tag{2.31}$$

It is worth noting that for a simple shorted slot ($Z_L = 0$) that is half of a wavelength long ($l = \frac{\pi}{\beta}$), the first mode dominates with a modal weight of $A_1 = 1$, while the next largest weight has a magnitude on the order of 10^{-3} according to Equation 2.28, so that the voltage distribution is reduced to

$$V_{half}(y) = V_0 cos(\beta y) \tag{2.32}$$

while for a full wavelength slot, ($l = \frac{2\pi}{\beta}$), the second mode dominates, reducing the voltage distribution to

$$V_{full}(y) = V_0 sin(\beta y). \tag{2.33}$$

The normalized ($V_0 = 1$) half-wavelength and full-wavelength slot voltage distributions are shown in Figure 2.2.

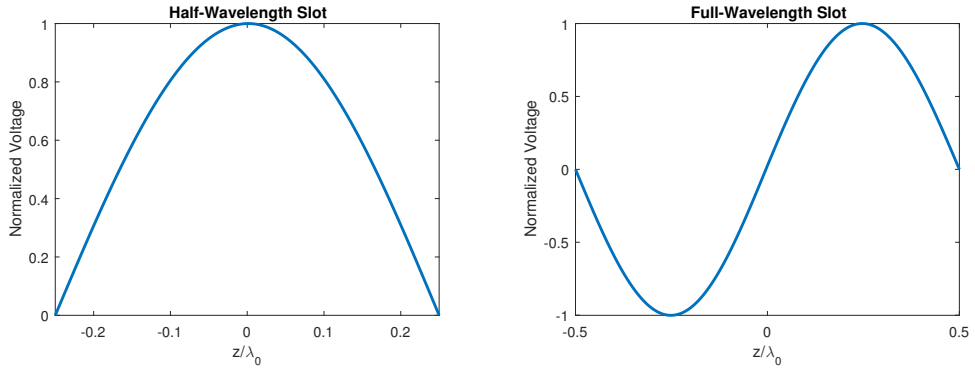

(a) (b)

Figure 2.2: Normalized voltage distributions calculated for (a) half- and (b) full-wavelength slots loaded with ideal shorts.

2.2 Radiation Pattern

The radiation pattern of a slot antenna can be calculated using the aperture field theory on the voltage distribution across the slot and by taking into account the edges of the ground plane. The effects of the finite ground plane can be evaluated by first calculating the radiated near-fields at the edges of the ground plane due to the slot antenna, then determining how those fields are diffracted. The method described in this section will be compared to simulation results from HFSS.

2.2.1 Near Field due to the Slot Aperture

In order to calculate the radiated near-fields of a slot antenna, it is first necessary to calculate the electric fields and the equivalent magnetic current density in the aperture of the slot. This can be accomplished using Laplace's equation [18] and the Field Equivalence Principle [19].

Assuming transverse electric and magnetic field modes [13], the electric field

across the slot aperture can be defined as

$$\mathbf{E} = \frac{V(y)}{w}\hat{\mathbf{x}} \tag{2.34}$$

where $V(z)$ is the voltage distribution across the slot as defined in Section 2.1.2, w is the width of the slot, and $\hat{\mathbf{x}}$ is the direction along the ground plane perpendicular to the length of the slot as shown in Figure 2.1. From the aperture field, the radiated near fields can be calculated using the Field Equivalence Principle and converting the aperture fields into equivalent magnetic current densities [19]. This theory uses boundary conditions on a perfect electric conductor (PEC) or a perfect magnetic conductor (PMC) to find initial currents, then removes the PEC or PMC using image theory to produce an equivalent current in free space. For a slot aperture, the electric field at the aperture turns into a magnetic current density as in

$$\mathbf{M} = -2\hat{\mathbf{n}} \times \mathbf{E} = 2\frac{V_0}{w}\hat{\mathbf{y}} \tag{2.35}$$

where $\hat{\mathbf{n}}$ is $\hat{\mathbf{y}}$. From the magnetic current density, the electric vector potential, F, can then be used. It is shown in [17], for magnetic surface current densities,

$$\mathbf{F} = \frac{\epsilon}{4\pi}\iint_{s'} \mathbf{M}\frac{e^{-j\beta R}}{R}ds' = F(R)\hat{\mathbf{y}} \tag{2.36}$$

where ϵ is the permittivity of the media, R is the distance from the point of integration to the observation point, and β is the phase constant. Using the electric vector potential, it is then relatively easy to calculate the radiating electric and magnetic fields with the equations

$$\mathbf{E} = -\frac{1}{\epsilon}\nabla \times \mathbf{F} = \frac{1}{\epsilon}\left(\frac{\delta F(R)}{\delta z}\hat{\mathbf{x}} - \frac{\delta F(R)}{\delta x}\hat{\mathbf{z}}\right) \tag{2.37}$$

and

$$\begin{aligned}\mathbf{H} &= -j\omega\mathbf{F} - \frac{j}{\omega\mu\epsilon}\nabla(\nabla\cdot\mathbf{F}) \\ &= -j\omega\mathbf{F} - \frac{j}{\omega\mu\epsilon}\left(\frac{\delta}{\delta x}\frac{\delta F(R)}{\delta y}\hat{\mathbf{x}} + \frac{\delta^2 F(R)}{\delta y^2}\hat{\mathbf{y}} + \frac{\delta}{\delta z}\frac{\delta F(R)}{\delta y}\hat{\mathbf{z}}\right)\end{aligned} \tag{2.38}$$

or, the magnetic field can be calculated from the electric field by using a far-field approximation,

$$\mathbf{H} = -\frac{1}{j\omega\mu}\nabla\times\mathbf{E} = \frac{-1}{j\omega\mu}\left(\frac{\delta E_z}{\delta y}\hat{\mathbf{x}} + \left(\frac{\delta E_x}{\delta z} - \frac{\delta E_z}{\delta x}\right)\hat{\mathbf{y}} - \frac{\delta E_x}{\delta y}\hat{\mathbf{z}}\right). \tag{2.39}$$

2.2.2 Far Fields over an Infinite Ground Plane

For an infinite ground plane, the edges of the ground plane do not need to be taken into account, so the far field radiation pattern can be calculated using only the magnetic current density across the slot. For aperture antennas, an approximation can be used that implements the $\mathbf{N}$ and $\mathbf{L}$ vectors based on Love's Equivalence Principle [19]. Only L is being used because all of the current densities on the slot are magnetic current densities, such that

$$E_r = 0 \tag{2.40}$$

$$E_\theta = -L_\phi\frac{jke^{-jkr}}{4\pi r} \tag{2.41}$$

$$E_\phi = L_\theta\frac{jke^{-jkr}}{4\pi r} \tag{2.42}$$

$$H_r = 0 \tag{2.43}$$

$$H_\theta = -L_\theta\frac{jke^{-jkr}}{4\pi\eta r} \tag{2.44}$$

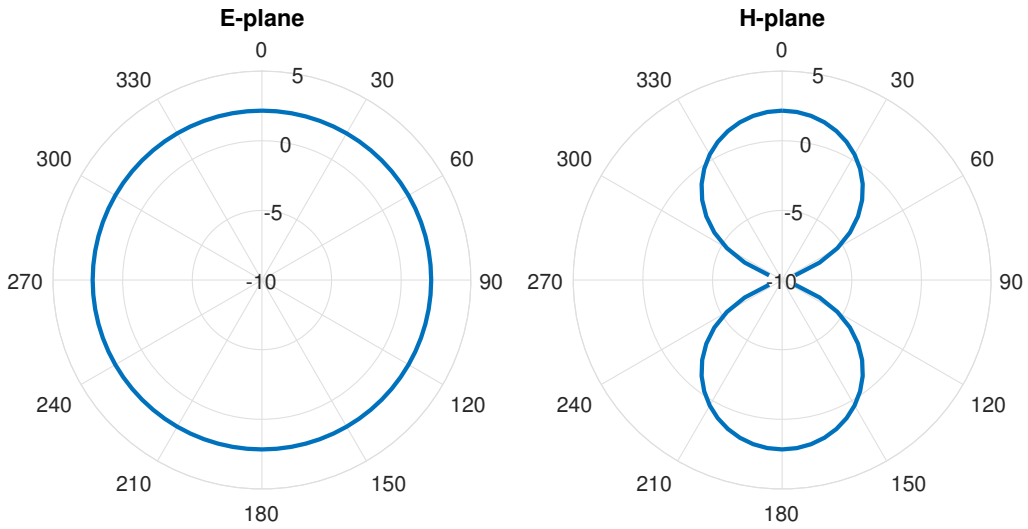

(a) (b)

Figure 2.3: Directivity (in dB) of a half-wavelength slot on an infinite ground plane.

$$H_\phi = L_\phi \frac{jke^{-jkr}}{4\pi\eta r} \tag{2.45}$$

where L is defined as

$$\mathbf{L} = \iint_{s'} \mathbf{M} e^{jkr'cos\psi} ds' \tag{2.46}$$

where k is the wave number, r and r' are the distances from the origin to the observation point and the aperture, respectively, η is the impedance of the surrounding media, and ψ is the angle from the aperture plane to the observation point. The peak directivity of the slot is 2.16 dB and has a null along the x-axis using the coordinate system shown in Figure 2.1.

The radiation pattern of a slot antenna on an infinite ground plane, shown in Figure 2.3, resembles that of a dipole antenna. This is because the slot antenna is a complementary antenna to the dipole [19], [20].

2.2.3 Far Fields over a Finite Ground Plane

By replacing the theoretical infinite ground plane with the physically realizable finite ground plane, edges are introduced that must be accounted for using the Uniform Theory of wedge Diffraction (UTD). This theory calculates the fields diffracted off of an edge and treats them as if they were their own radiation sources adding to the original source [21]. Because of this, the radiation effects due to the edges of the ground plane can be modeled as equivalent currents on the edges and incorporated into the radiation pattern calculation.

From UTD, the fields diffracted from a conducting edge due to an incident field are

$$E_v = D_{||} E_v^i \frac{e^{-j\beta r}}{\sqrt{r}} \tag{2.47}$$

and

$$H_v = D_{\perp} H_v^i \frac{e^{-j\beta r}}{\sqrt{r}} \tag{2.48}$$

as shown in Figure 2.4 where E_v^i and H_v^i are the v-polarized electric and magnetic fields incident at the edge, calculated using Equations 2.37 and 2.39, r is the distance from the edge point Q to the observation point P, β is the phase constant, and $D_{||}$ and $D_{\perp}$ are the parallel and perpendicular scalar diffraction coefficients. These coefficients are dependent on the distance from the edge, the angle of the source, and the angle of observation and can be calculated as shown in [21]. While they edges can be modeled as equivalent currents on the edges, they are not really there. The diffraction is due to a discontinuity in the ground plane, not a high concentration of current along the edges [21].

Using a Hankel function approximation [21], it can be shown that the electric

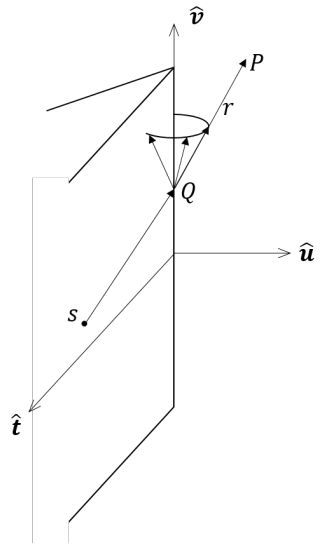

Figure 2.4: Diffracted fields at edge point Q from source point s on an edge along the $\hat{\mathbf{v}}$ axis.

fields produced by an electric current, I^e, are

$$E_v = \eta\beta I^e \frac{e^{j\frac{\pi}{4}}}{2\sqrt{2\pi\beta r}} e^{-j\beta r} \tag{2.49}$$

and, similarly, the magnetic fields produced by a magnetic current, I^m, are

$$H_v = -\frac{\beta}{\eta} I^m \frac{e^{j\frac{\pi}{4}}}{2\sqrt{2\pi\beta r}} e^{-j\beta r}. \tag{2.50}$$

By then combining Equations 2.49 and 2.50 with Equations 2.47 and 2.48, equivalent electric and magnetic currents can be derived as [21]

$$I^e = \frac{-2j}{\eta\beta} E_z^i D_{||} \sqrt{2\pi\beta} e^{j\frac{\pi}{4}} \tag{2.51}$$

and

$$I^m = \frac{2j\eta}{\beta} H_z^i D_{\perp} \sqrt{2\pi\beta} e^{j\frac{\pi}{4}}. \tag{2.52}$$

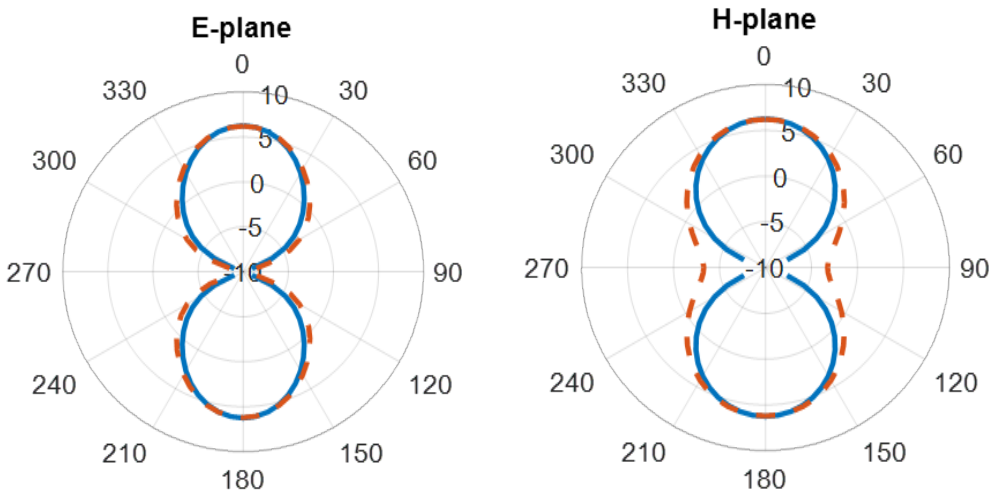

(a) (b)

Figure 2.5: Directivity (in dB) of a half-wavelength slot lying in the x-y plane on a finite ground plane. UTD method (blue solid line) compared to HFSS results (red dotted line).

For a slot antenna, the electric fields due to the aperture are always perpendicular to the ground plane, so there is no equivalent electric current.

For the entire structure, a similar method to that of the far field pattern for the infinite ground plane can be used. First, the equivalent magnetic currents from diffraction on the edges of the ground plane for each side must be found using Equation 2.52. Then, by including the edge diffraction currents in the integration in Equations 2.46, and following through with Equations 2.40 to 2.45, the far field pattern of the slot antenna on a finite ground plane can be obtained. As shown in Figure 2.5, the radiation pattern for a slot antenna on a finite ground plane has a null on the entire x-y plane, instead of only along the x-axis as it is for an infinite ground plane. The directivity is also increased from 2.16 dB to 6.251 dB.

It is also worth noting that where the slot antenna is placed on the ground plane has an effect on its radiation pattern. Figure 2.6 shows the E-plane of the radiation pattern for three slots offset from the center of the ground plane. Therefore, it

cannot be assumed that the radiation patterns of several slots on the same ground plane have similar radiation patterns, since they will all be in different locations on the ground plane.

2.3 Conclusions

In this chapter, it was shown that the input impedance and voltage distribution of a single slot antenna on a finite ground plane could be accurately modeled using lossy transmission line theory. Additionally, a method for calculating the three dimensional radiation pattern of a slot antenna on a finite ground plane was established using UTD. This model can not only be used with a simple, shorted slot configuration, but it can also take into account slot antennas with complex end loads, such as the ring resonator end loads of the RRELSA. In later chapters, this model will be used to determine the input impedances and radiation patterns of the individual elements in the array.

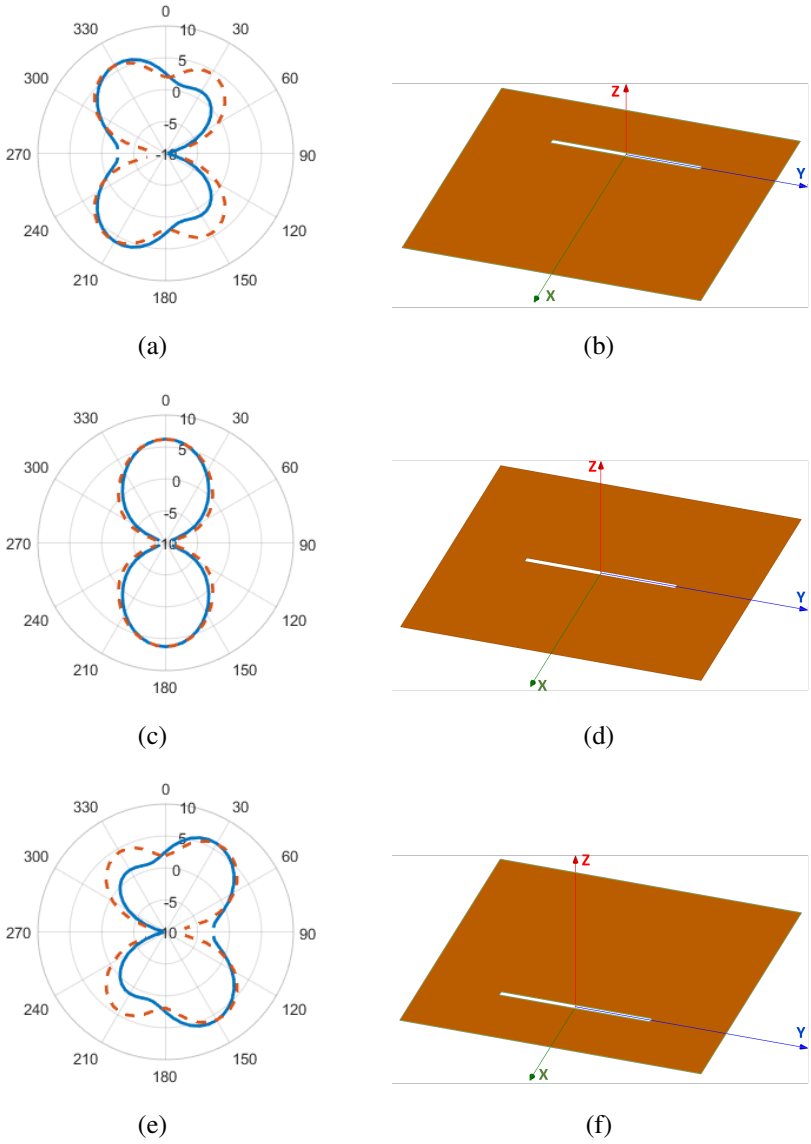

Figure 2.6: Directivity (in dB) in the E-plane of a half-wavelength slot lying off-center in the x-y plane on a finite, square ground plane that has a side length of λ. The calculated radiation pattern using UTD (blue line) is compared to an HFSS simulation (red line). The slot is shifted in the x direction by (a,b) -λ/4, (c,d) λ/4, and (e,f) 0, for comparison

Chapter 3

Ring Resonator End Loaded Slot Antenna (RRELSA)

The Ring Resonator End Loaded Slot Antenna (RRELSA) was originally designed by Lukasz Szolc [2], a fellow Graduate Research Assistant at the University of Oklahoma. The RRELSA is a frequency reconfigurable antenna that can be continuously tuned using a DC bias line. This chapter serves to characterize the basic design of RRELSA for its use in a pattern reconfigurable array, as discussed in Chapter 5. Additionally, it develops the theory of the antenna so that the RRESLA can be redesigned for different frequency ranges.

3.1 Original Design

The original design of the antenna according to Szolc [2], had a slot length of 53 mm, width of 3 mm, and a ring resonator radius of 3 mm. The varactors used were the hyperabrupt varactor diodes, SMV1405-040LF. The width of the ring resonator slot was designed so that the varactors could be placed across it, about 0.4 mm. This varactor ranged from 0.5 to 2.54 pF with a voltage range of 0 to 30 Volts. It was fed with a 90 degree radial stub with a microstrip impedance of 25 Ohm underneath the slot. The microstrip line tapers down to a 50 Ohm line at the edge of the ground plane where a coaxial cable is attached, shown in Figure 3.2. The

bias lines implemented were thin microstrip lines attached with a via. The ring resonators were then attached to a DC voltage generator to bias the antenna.

With this setup, the antenna could continuously be tuned from 1.65 to 2.9 GHz. Figure 3.1 shows the reflection coefficient and the peak radiation gain of the RRELSA.

3.2 Theory of Design

The RRELSA was designed as a single slot antenna, fed by a radial microstrip stub and loaded on each end with a ring resonator, as shown in Figure 3.2. The ring resonators were biased using lines on the backside of the ground plane so that the end loads could be tuned with a DC voltage [2].

The basic design of the RRELSA centered on operating at the second resonance of a slot antenna, which creates a low impedance point at the center of the slot with a low voltage and high current [2]. As the slotline extends from the center point, the impedance becomes capacitive until a quarter wavelength away where the impedance is maximized and becomes and open circuit [15]. For a slotline greater than a quarter wavelength, the impedance is inductive until it has another low impedance point a half wavelength away from the center. In order to satisfy the boundary conditions of the second resonance on the slot, the impedance at the end of the slot must match the impedance at that point [13]. For a slot antenna operating at the second resonance, this is typically done by truncating the slotline with a short a half wavelength away from the center, creating a full-wavelength slot. The RRELSA, on the other hand, places its ring resonator end load about a sixth of a wavelength from the center while biasing the end loads to be capacitive [2]. As the ring resonators were tuned to different impedances, the boundary condition at

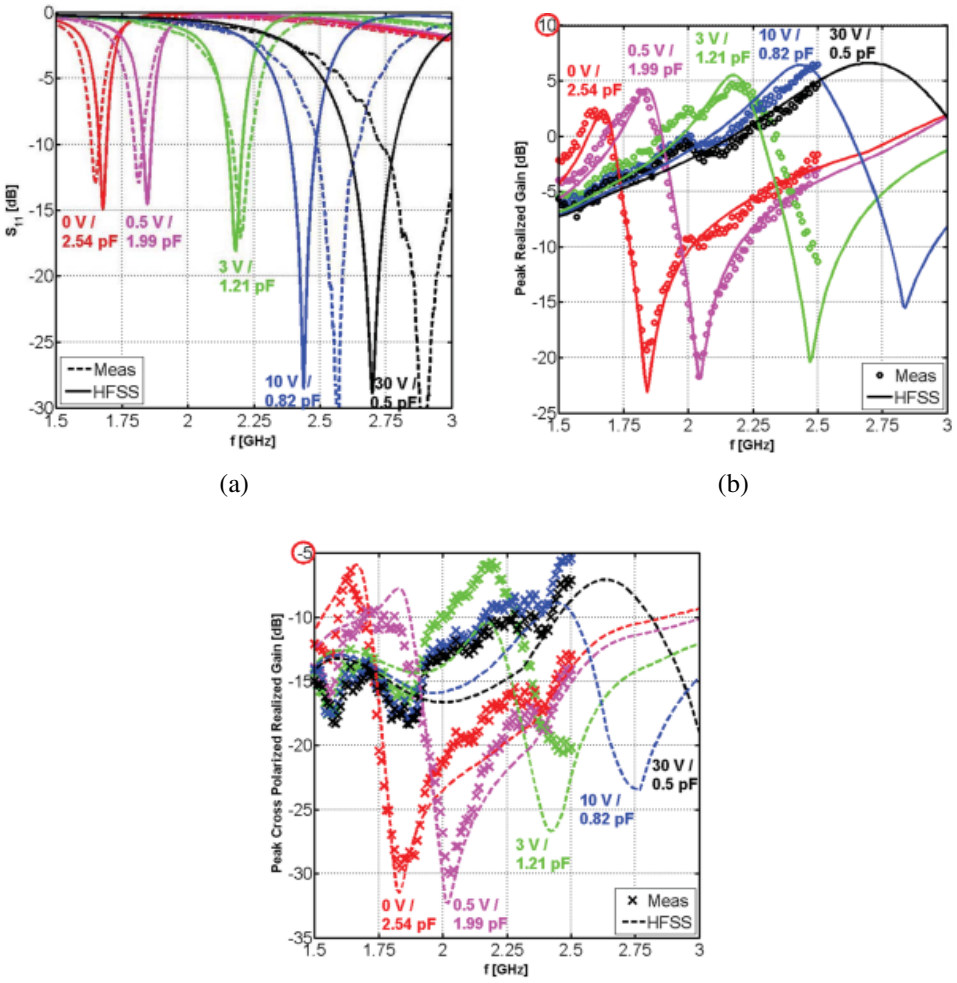

(a) (b)

(c)

Figure 3.1: (a) Reflection coefficient, (b) peak gain, and (c) cross polarized gain of the Ring Resonator End Loaded Slot Antenna across frequency for different voltage biasing [2].

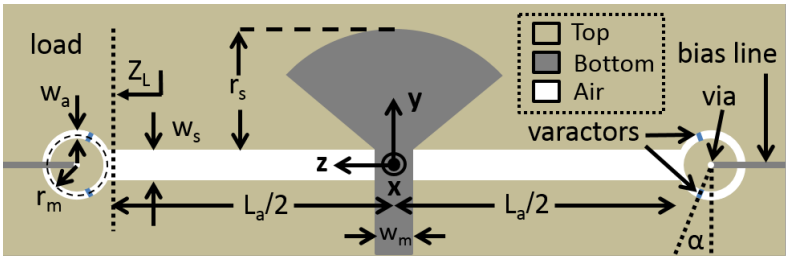

(a)

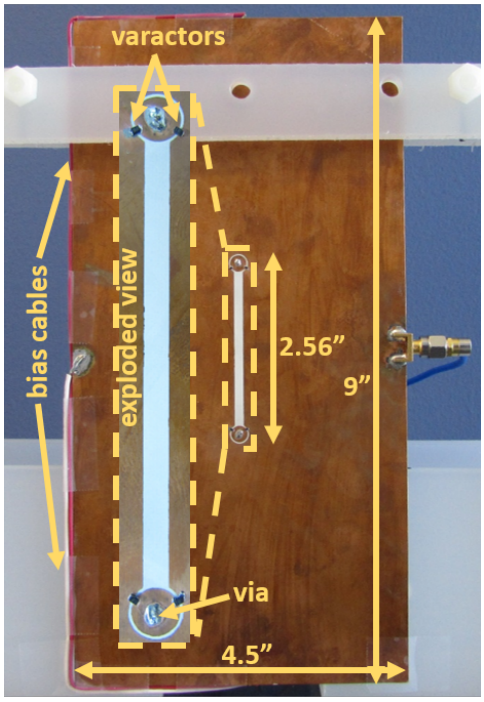

(b)

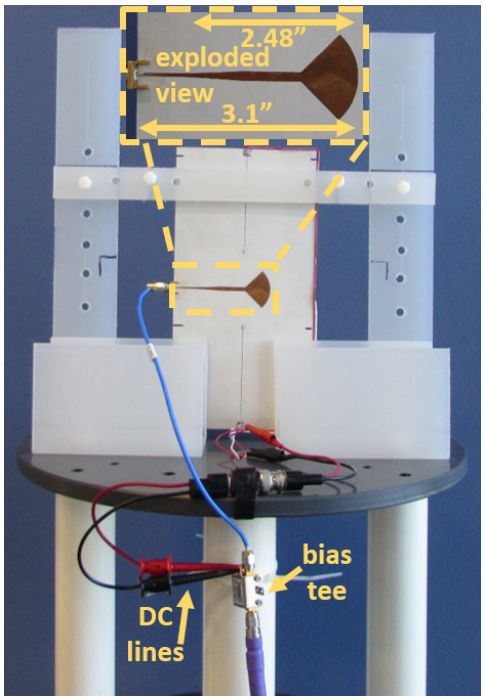

(c)

Figure 3.2: Initial design of the Ring Resonator End Loaded Slot Antenna [2]. Shown is (a) graphic model, (b) the front and (c) the back of the fabricated antenna along with the mounting device used during measurement. The RRELSA is connected to the AC generator with a bias tee to prevent DC power from flowing back to the AC generator.

the end of the slot changed, exciting different frequencies.

The input impedance and radiation pattern are similar to that of a traditional, shorted slot antenna and can be calculated using the methods discussed in Section 2.1.

3.3 End Load Design

The end loads of the slot needed to be able to take on a wide range of impedances, so the initial design was a reconfigurable resonator [2]. In particular, a slot ring resonator loaded with varactors was used, shown in Figure 3.3.a, that could be reconfigured with a DC bias line, which will be discussed in Section 3.4. The capacitance of the varactors effectively increase the circumference of the ring resonator, changing the electrical length so that resonances shift in frequency. The varactors change capacitance with a voltage bias, so the DC bias line enables control over the resonances of the ring resonator [2].

In order to find the input impedance of the ring resonator, the structure can be temporarily modeled as a straight slotline with intermittent capacitive loads [2]. The capacitors, set at angles ϕ_1 and ϕ_3 from the radiating slot aperture, split the resonator into three different lines of lengths l_1, l_2, and l_3 and width w_L. By then using ABCD parameters, the three lines and the capacitors can be cascaded to obtain the network parameters of the entire line. The ports of the system are then looped back on each other to model the loop structure, shown in Figure 3.3.b. The input admittance and impedance can be easily obtained by converting the network parameters into an equivalent pi-network, Figure 3.3.c, so that

$$Y_{in} = \frac{1}{Z_{in}} = \frac{Y_1 Y_2}{Y_1 + Y_2} + Y_3. \tag{3.1}$$

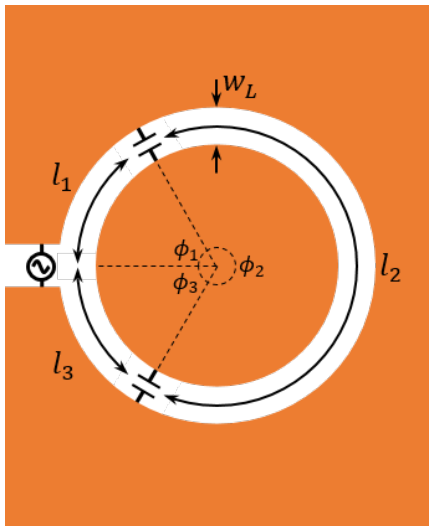

(a)

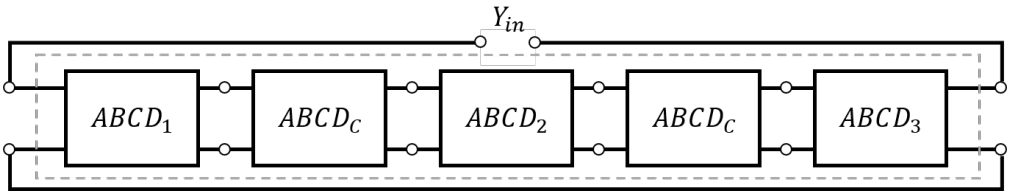

(b)

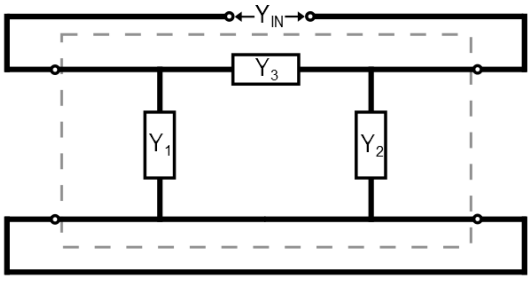

(c)

Figure 3.3: Physical (a), matrix (b), and circuit (c) model of the slot ring resonator loads implemented at the ends of the RRELSA. The ring resonator can be modeled as a slotline split into three lengths, l_1, l_2, and l_3, by the varactors. By cascading the three transmission lines and two varactors using ABCD parameters (b) and using an equivalent pi-network (c), the input impedance can be calculated.

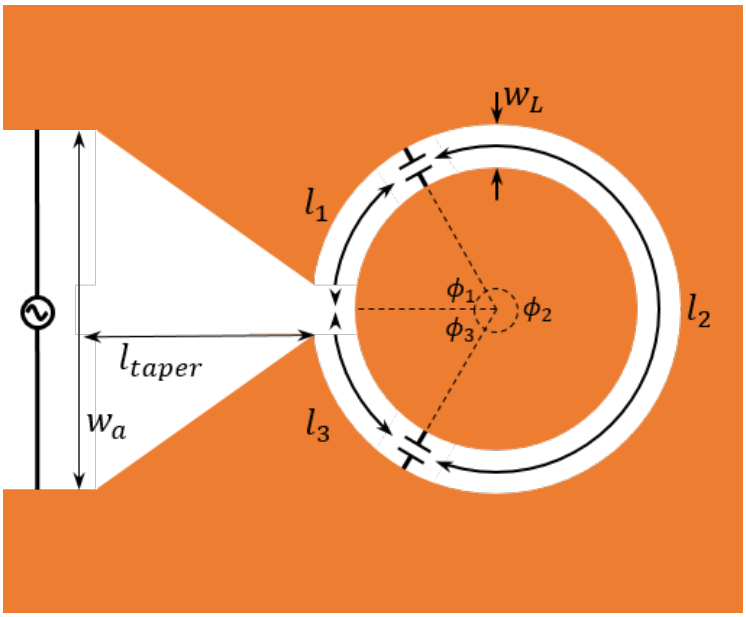

Figure 3.4: Redesigned slot ring resonator featuring a taper to improve the accuracy of the model. The wide aperture of the main radiating slot aperture, w_a, is tapered down to a small input port over a length of l_{taper} to better model the ring resonator.

In the original design, Szolc connected the resonator directly to the slot, but still took into account the entire 2π radians of the ring resonator [2]. This approximation made the ring resonator model inaccurate. To resolve this issue, the ring resonator was redesigned to have the full circle come down to a small opening (less than half a millimeter), then taper out to merge with the main slot of the antenna, as shown in Figure 3.4. The taper could be modeled using a stair step approach of increasing slot widths and cascading the ABCD parameters. This enabled the ring resonator model to be more robust and accurate when loaded onto the RRELSA.

Using the above method, the slot ring resonators can be designed for a specific width and radius depending on the desired frequency and the available capacitance values on the varactor. In this design, it is important to note that the varactors can only add capacitance to the structure, effectively lengthening the circumference of the ring resonator. This means that the smallest effective circumference of the

varactor loaded ring resonator is the physical circumference. This imposes a hard limit on the highest frequency the RRELSA is able to tune to. For this reason, it is important to design the ring resonator with the highest desired frequency in mind.

3.4 Bias Line

In order to tune the end loads and reconfigure the RRELSA, bias lines need to be implemented to the inner circle of the slot ring resonator. With the rest of the copper plate DC grounded, the bias line will put a voltage across the varactors, changing their capacitance and tuning the operating frequency of the antenna. Care must be taken in the design and placement of the bias lines so that AC power from the antenna does not flow back on the lines and reach the DC generators and so that they do not disturb the radiation pattern.

3.4.1 Microstrip Bias Line

In the original design, a thin microstrip line ran along the underside of the substrate and connected with the inner conductor of the ring resonator with a via. The thin bias lines were implemented with a high impedance of over 90 Ω so that the abrupt impedance change would cause reflections in high frequencies [2], minimizing the AC power flowing back toward the DC generators. They were additionally placed in the null of the radiation pattern to minimize its effect on the radiative properties of the antenna, shown previously in Figure 3.2 [2]. While this is a usable solution, the necessity of vias in the design makes it difficult to fabricate.

3.4.2 Coplanar Waveguide Bias Line

Coplanar waveguide bias lines were further investigated as a potential solution to more easily fabricate the array; no vias are needed and it uses a simpler multilayer alignment. Unfortunately, a high impedance line cannot be used to prevent AC power on the line because it would disturb the current flow on the ground plane too much. Bandstop filters could instead be implemented along the lines. First order ideal bandstop filters have a narrow bandwidth, requiring many different first-order filters to cover the entire bandwidth. Non-ideal filters, however, created using interdigital bandstop filters on the coplanar waveguide have harmonics which could be strategically designed to cover the entire bandwidth. Using this method, fewer individual bandstop filters are needed along the line to filter 0.7 to 7 GHz from traveling along the bias lines. A total of seven filters, designed at 0.7, 0.9, 1.3, 1.5, 2.2, 2.65, and 4.3 GHz, were needed to block the large spectrum. No further filters were needed for the higher frequencies because they were blocked by harmonics of the lower frequency filters. Additionally, in order to condense the total length of the filter, two different types of coplanar bandstop filters were used: an inner folded filter and an outer inductive filter. This enabled the individual filters to be placed much closer together. The filter was fabricated and the results are shown in Figure 3.5. As can be seen in the figure, the coplanar waveguide bias line filter provides about 30 dB of attenuation across the desired bandwidth from 0.7 to 7 GHz.

Ultimately, this bias line was not suitable for this antenna. The coplanar filters designed were about 200 mm long which is too big to be used in a compact antenna. Additional research will need to be done to make the line more compact, but for now the microstrip bias lines will be used in the antenna designed here.

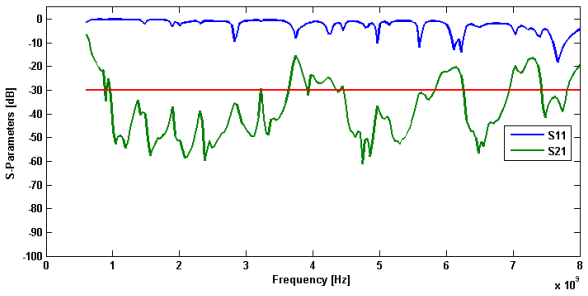

(a) S-Parameters

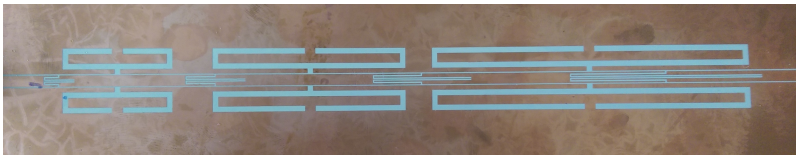

(b) Fabricated Filter

Figure 3.5: S-Parameters and picture of the fabricated bandstop filter.

3.5 Feeding Network

A microstrip-coupled feed is one of the most common methods to feed a slotline or slot antenna [2], [22]. It has the advantage of having a very low profile, has a small size, and can have a large bandwidth depending on its implementation. Instead of driving a voltage difference across the slot, it couples into the near fields of the slot, which can be modeled as an ideal transformer that can increase the input impedance of the antenna, discussed later in this section. For this reason, while the feed can be designed to be placed anywhere on the slot antenna, it is most effective when placed near a voltage minimum where the impedance of the slot antenna is naturally low [23].

In general, the goal in designing a microstrip-coupled feed is to design a current maximum on the microstrip line where it intersects with the slot antenna. Ideally, this point on the slot antenna would also be a voltage minimum or current maximum to ensure strong magnetic field coupling between the two structures. While

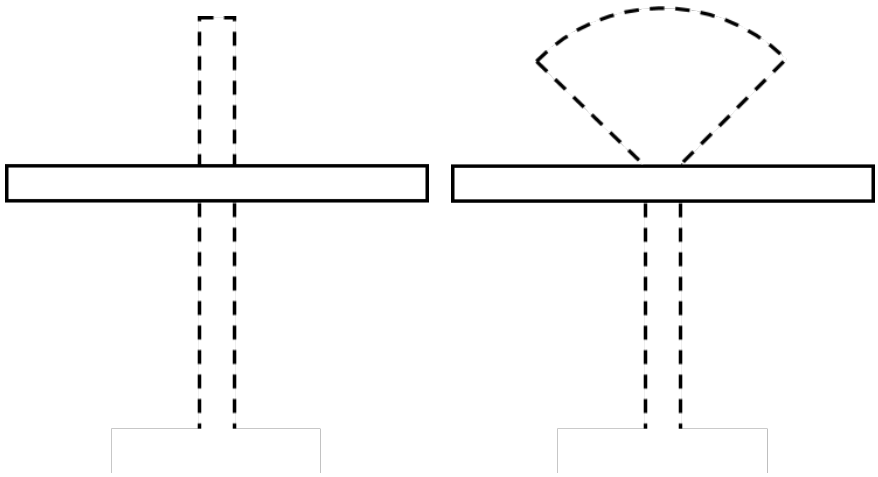

Figure 3.6: Microstrip feed (dotted line) underneath a slot antenna (solid line). (a) straight stub, (b) radial stub

the current minimum under the slot on the microstrip line can be implemented several ways, it is typically achieved by extending the microstrip line a quarter of a wavelength past the slotline, as shown in Figure 3.6.a. This is a fairly narrowband solution because of the quarter wavelength stub, but it can be made more broadband by turning the straight stub into a radial stub [24], [25], shown in Figure 3.6.b. Another way to achieve a virtual current maximum underneath the slot is to short the microstrip line to the far edge of the slot with a via. While shorting the feed line does not place the effective short directly underneath the slot, it is more broadband, takes up less space, and is easier to model [26]. The radial stub is used in the original design of the RRELSA, but the shorted microstrip line will be used in later designs.

The coupling between a microstrip line and a slot antenna can be modeled as a n:1 transformer, as shown in Figure 3.7 [27], [28]. With the input impedance of the slot antenna, $Z_{in,slot}$, already calculated in Section 2.1.1, the impedance seen at the

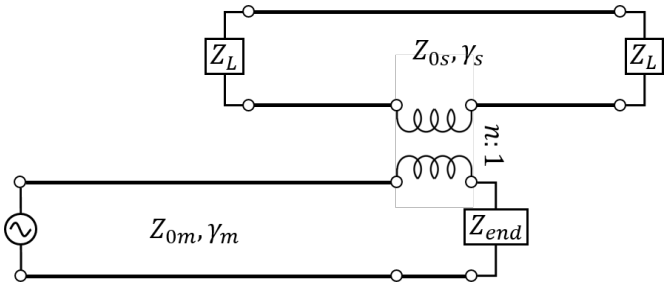

(a)

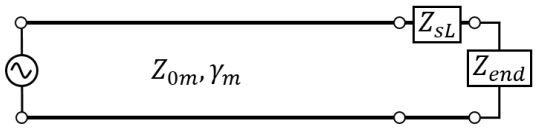

(b)

Figure 3.7: Model of the microstrip-coupled slot antenna(a) with a transformer and (b using an equivalent series impedance of the slot antenna, Z_{sL}.

other end of the transformer as a series impedance on a microstrip line, Z_{sL}, is

$$Z_{sL} = \frac{Z_{in,slot}}{n^2} \tag{3.2}$$

where n can be approximated using

$$n = \sqrt{\frac{L_m}{L_s}} \tag{3.3}$$

and where L_m and L_s are the characteristic inductances of the microstrip and slot [29], respectively which can be calculated by using the characteristic impedance with Equation 2.5. Figure 3.8 compares HFSS simulation results with the circuit model described in this section and shows agreement at the frequency of operation. The equivalent series impedance can then be added to the impedance of the end of the microstrip line and treated as a lumped load impedance at the end of a microstrip line. Then the microstrip line can be tapered to match the port impedance of the system, typically 50 Ω.

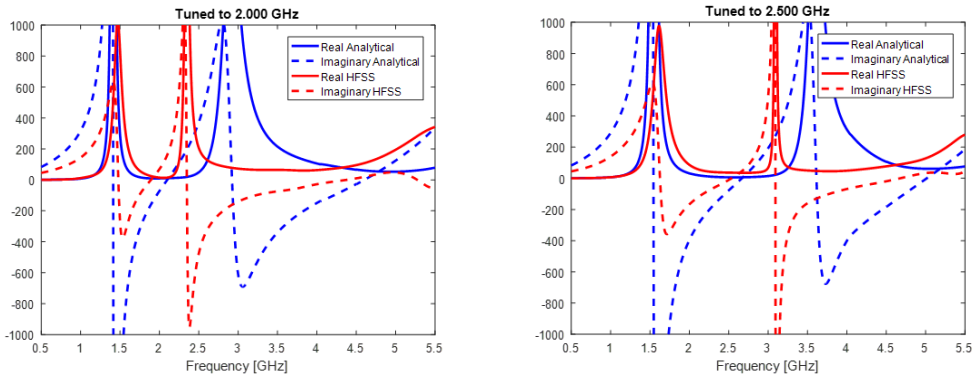

(a) (b)

Figure 3.8: Impedance seen at the microstrip feed line, Z_{sL}, due to the RRELSA tuned to different frequencies. Circuit model method (blue solid line) compared to HFSS results (red dotted line).

3.6 Conclusions

In this chapter, the RRELSA was shown to be frequency reconfigurable and able to be tuned with a simple DC bias. The RRELSA was also modeled as a function of wavelength so that the antenna could be designed for different frequency ranges. The ring resonators were similarly characterized so that they could be designed for a particular frequency range given the set of possible capacitance values of the varactor. Two methods of biasing the ring resonators were discussed: the microstrip and coplanar bias lines. While the coplanar bias line had the benefit of being in the same plane as the antenna, its required size made it difficult to implement, so the microstrip bias line was used instead. The feeding network to the original RRELSA was also designed to be a microstrip-coupled feed with a radial stub [2], but in future designs a via short to the ground plane will be implemented as a more broadband solution. With the design of the RRELSA established, it becomes possible to implement the antenna as an element in a reconfigurable array.

Chapter 4

Linear Yagi-Uda Style Arrays

In order to achieve pattern reconfigurability, a Yagi-Uda style array, shown in Figure 4.1, was chosen to direct the radiation from the RRELSA. This type of array can use as little as three elements and directs the radiation using passive elements instead of active ones. Although the RRELSA design has been established and various parameters, such as input impedance and voltage distribution, has been defined in previous chapters, it has not yet been shown how multiple antennas interact with each other in an array. In this chapter, linear array theory is established and the coupling between multiple antennas is calculated. Additionally, the input impedance and total radiation pattern to a Yagi-Uda array is derived using network parameters and array factor.

4.1 Element Design

The elements in a Yagi-Uda array take on different roles depending on their size and relative location. Each element has a different role and should be designed differently. Generally, they can be initially designed based on a Yagi-Uda design table, such as the one shown in Figure 4.2. In a standard Yagi-Uda array, these elements are fixed and cannot be changed. If they were designed to be reconfigurable,

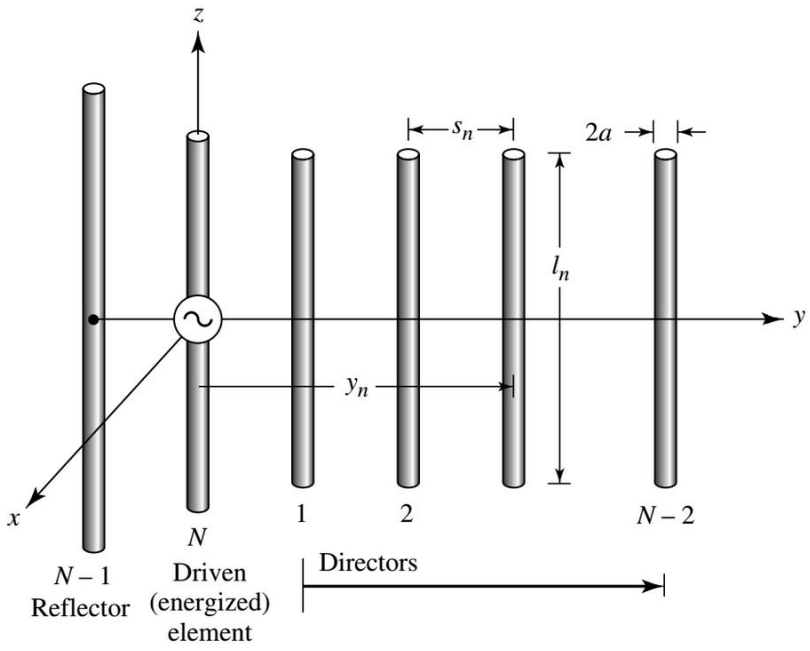

Figure 4.1: Design table for Yagi-Uda antennas from [19]

however, they could potentially take on different roles in the array.

The driven element is the only element that is attached to the signal generator. It is the primary resonator of the array and has the largest influence on the overall input impedance, so it should be designed to be resonating and impedance matched at the frequency of interest. For an unloaded linear antenna, such as a dipole or slot antenna, this means having a length close to an integer multiple of half a wavelength.

The reflector in a Yagi-Uda array is an element similar to the driven element, but it is electrically longer. It does not greatly affect the input impedance of the array, but instead couples to the driven element and "pushes" the radiation pattern away from it. Typically, there is only one reflector in a Yagi-Uda array, but more can be added with little overall influence on either the input impedance or radiation pattern.

$d/\lambda = 0.0085$		Length of Yagi-Uda (in wavelengths)					
$s_{12} = 0.2\lambda$		**0.4**	**0.8**	**1.20**	**2.2**	**3.2**	**4.2**
LENGTH OF REFLECTOR (l_1/λ)		**0.482**	**0.482**	**0.482**	**0.482**	**0.482**	**0.475**
LENGTH OF DIRECTORS, λ	l_3	0.442	0.428	0.428	0.432	0.428	0.424
	l_4		0.424	0.420	0.415	0.420	0.424
	l_5		0.428	0.420	0.407	0.407	0.420
	l_6			0.428	0.398	0.398	0.407
	l_7				0.390	0.394	0.403
	l_8				0.390	0.390	0.398
	l_9				0.390	0.386	0.394
	l_{10}				0.390	0.386	0.390
	l_{11}				0.398	0.386	0.390
	l_{12}				0.407	0.386	0.390
	l_{13}					0.386	0.390
	l_{14}					0.386	0.390
	l_{15}					0.386	0.390
	l_{16}					0.386	
	l_{17}					0.386	
SPACING BETWEEN DIRECTORS (s_{ik}/λ)		0.20	0.20	0.25	0.20	0.20	0.308
DIRECTIVITY RELATIVE TO HALF-WAVE DIPOLE (dB)		7.1	9.2	10.2	12.25	13.4	14.2
DESIGN CURVE (SEE FIGURE 10.27)		(*A*)	(*B*)	(*B*)	(*C*)	(*B*)	(*D*)

Figure 4.2: Design table for Yagi-Uda antennas from [19]

The final element in the typical Yagi-Uda array is the director. It is similar to the reflector in that it primarily changes the radiation pattern of the array and not the input impedance, but instead of ”pushing” the radiation pattern away, it ”pulls” it toward itself. Also, while there can be only one director in an array, many can also be used and each additional director greatly increases the directivity of the array. For that reason it is common to see Yagi-Uda antennas with six or more directors.

In general, the spacing between the elements should be a little shorter than a quarter of a wavelength, about 0.2λ. This is not necessarily the optimal spacing for all arrays, and in typical Yagi-Uda arrays the spacing is first determined with a design table (Figure 4.2), then optimized using a full-wave solver.

4.2 Coupling

The effect of the reflector and directors on the input impedance and radiation pattern of the array can be analyzed and accounted for using an equivalent network matrix. Each element is modeled as having a port in the center which can be loaded or connected to a generator. The matrix can be calculated using using methods discussed in this section.

4.2.1 Transmission Line Even/Odd Mode Coupling

If the elements in the array can be modeled as end-loaded transmission lines, one method of calculating the network matrix of the array is to use even and odd mode impedances. Using these transmission line coupling impedances, the overall impedances relating the unloaded transmission lines can be calculated. As shown from Paul Winniford’s work [30], the impedance matrix of three unloaded trans-

mission lines takes the form

$$[Z] = \begin{bmatrix} Z_{11}e^{-\gamma 0} & Z_{11}e^{\gamma 0} & Z_{12}e^{-\gamma 0} & Z_{12}e^{\gamma 0} & Z_{13}e^{-\gamma 0} & Z_{13}e^{\gamma 0} \\ Z_{21}e^{-\gamma 0} & Z_{21}e^{\gamma 0} & Z_{22}e^{-\gamma 0} & Z_{22}e^{\gamma 0} & Z_{23}e^{-\gamma 0} & Z_{23}e^{\gamma 0} \\ Z_{31}e^{-\gamma 0} & Z_{31}e^{\gamma 0} & Z_{32}e^{-\gamma 0} & Z_{32}e^{\gamma 0} & Z_{33}e^{-\gamma 0} & Z_{33}e^{\gamma 0} \\ Z_{31}e^{-\gamma l} & Z_{31}e^{\gamma l} & Z_{32}e^{-\gamma l} & Z_{32}e^{\gamma l} & Z_{33}e^{-\gamma l} & Z_{33}e^{\gamma l} \\ Z_{21}e^{-\gamma l} & Z_{21}e^{\gamma l} & Z_{22}e^{-\gamma l} & Z_{22}e^{\gamma l} & Z_{23}e^{-\gamma l} & Z_{23}e^{\gamma l} \\ Z_{11}e^{-\gamma l} & Z_{11}e^{\gamma l} & Z_{12}e^{-\gamma l} & Z_{12}e^{\gamma l} & Z_{13}e^{-\gamma l} & Z_{13}e^{\gamma l} \end{bmatrix} \tag{4.1}$$

where Z_{mn} is the impedance between ports m and n calculated in [30], l is the distance from the port to the end of the transmission line, and γ is the propagation constant on the line. This matrix shows the multiline Z-parameters of a 6-port system implemented in the diagram show in Figure 4.3. With the center transmission line driven by a generator, two impedance matrices can be cascaded, one on either end, and loaded with different load impedances depending on the particular element used.

Unfortunately, the even and odd mode impedance evaluation only takes the near field between transmission lines into account. For most Yagi-Uda arrays, the spacing between transmission lines is too large to be considered near field. Because

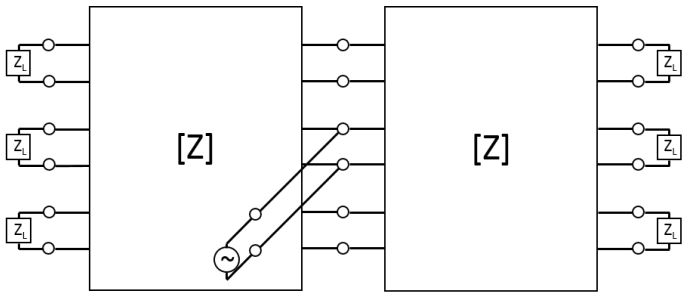

Figure 4.3: Diagram depicting how the impedance matrix will be used. Two matrices will be cascaded with the center transmission line being fed and the ends of the lines having reconfigurable loads.

the element transmission lines are antennas and radiating, this method neglects the coupling due to that radiation.

4.2.2 Radiative Coupling

Instead of using a transmission line coupling model, a more accurate coupling model would be to find the coupling due to the radiated far-fields of the antennas. The radiated power from a generator-driven antenna induces a current or voltage across a nearby antenna that is then re-radiated. The coupled power can be modeled as an equivalent impedance or admittance between the two antennas. Then, using the mutual and self impedances or admittances, an equivalent network matrix can be formed. The use of network matrices allows the model to include any number of elements in the array. Shown below is the derivation of the network matrix for a two element array, but it can be expanded as needed.

For example, in the case of a dipole, a current source is placed at the port and induces a voltage difference between the two arms in relation to its self impedance, $V = ZI$. For two dipoles coupled together, as shown in Figure 4.4.a, the voltage across one of the dipoles has to take into account the current on the other dipole as well as its own current. The voltage equation then takes the form of impedance parameters:

$$V = Z_{self} I_{self} + Z_{mutual} I_{other} \tag{4.2}$$

where V is the voltage across the slot, Z_{self} is the self impedance of the dipole, Z_{mutual} is the mutual impedance between the dipoles, and I_{self} and I_{other} is the current on the dipole and the coupled dipole, respectively. The set of voltage equations

for each of the dipoles can be combined in a matrix form as

$$\begin{bmatrix} V_1 \\ V_2 \end{bmatrix} = \begin{bmatrix} Z_{11} & Z_{12} \\ Z_{21} & Z_{22} \end{bmatrix} \begin{bmatrix} I_1 \\ I_2 \end{bmatrix} \tag{4.3}$$

where V_n and I_n are the voltage and current on the nth dipole and Z_{nm} is defined as

$$Z_{nm} = \left. \frac{V_n}{I_m} \right|_{I_k=0, k\neq m}. \tag{4.4}$$

Therefore for the first dipole,

$$Z_{11} = \left. \frac{V_1}{I_1} \right|_{I_2=0} = Z_{1,self} \tag{4.5}$$

so the diagonal of the impedance matrix can be used for the primary diagonal of the impedance matrix. For slot antennas, admittance parameters are used and a similar matrix can be formed as

$$\begin{bmatrix} I_1 \\ I_2 \end{bmatrix} = \begin{bmatrix} Y_{11} & Y_{12} \\ Y_{21} & Y_{22} \end{bmatrix} \begin{bmatrix} V_1 \\ V_2 \end{bmatrix} \tag{4.6}$$

and similarly the main diagonal of the matrix can be determined by the self admittance of the individual slot antenna.

There are a couple of methods of obtaining the mutual impedance or admittance between two antennas [31], such as the antennas shown in Figure 4.4. The first method involves using the reciprocity theorem and circuit relations to find the induced voltage across the port of one antenna due to the electric field generated by the other. According to this method, the mutual impedance of two dipoles can be

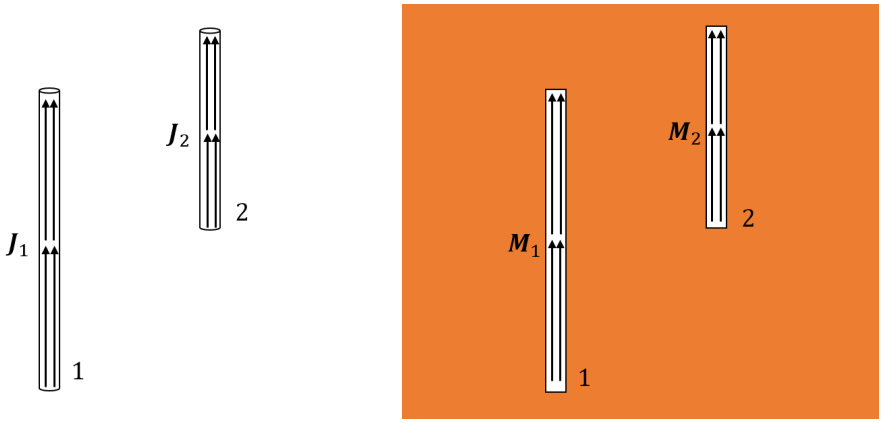

(a) (b)

Figure 4.4: Adjacent dipoles (a) and slot antennas (b) that couple into each other with far-field radiation.

calculated by

$$Z_{12} = \frac{V_{12}}{I_2} = \frac{-1}{I_1 I_2} \iint_{S_2} \mathbf{E}_{21} \mathbf{J}_2 dS_2 \tag{4.7}$$

where V_{12} is the voltage induced at port 1 by dipole 2, $\mathbf{E}_{21}$ is the electric field at dipole 2 due to dipole 1, $\mathbf{J}_2$ is the electric current density on dipole 2, I_1 and I_2 are the currents at the ports of dipoles 1 and 2. Similarly, for a slot antenna, the mutual admittance can be calculated using

$$Y_{12} = \frac{I_{12}}{V_2} = \frac{-1}{V_1 V_2} \iint_{S_2} \mathbf{H}_{21} \mathbf{M}_2 dS_2 \tag{4.8}$$

where I_{12} is the current induced at port 1 by slot 2, $\mathbf{H}_{21}$, the magnetic field at slot 2 due to slot 1, $\mathbf{M}_2$ is the magnetic current density on slot 2, V_1 and V_2 are the voltages at the ports of slots 1 and 2. This method was originally published to calculate the mutual impedance of straight dipoles and slot antennas with a sinusoidal current distribution and a small cross section [31].

The other primary method to calculate the mutual impedance between antennas is called the Induced EMF Method [31]. It was designed to calculate the self

and mutual impedances of small antennas with a uniform current distribution. This method uses basic field theory with transmission line theory to calculate the induced power on one antenna based on another. It starts with the expression for electromagnetic power over two antennas and equates it to the voltages and currents on the antennas:

$$\mathbf{S} = \iint_{S_1 S_2} (\mathbf{E} \times \mathbf{H}^*) dS_1 dS_2 = - \iint_{S_1 S_2} \mathbf{E}\mathbf{J}^* dS_1 dS_2 = V_1 I_1^* + V_2 I_2^* \tag{4.9}$$

where $\mathbf{S}$ is complex electromagnetic power, $\mathbf{E}$ and $\mathbf{H}$ are the electric and magnetic field intensities in a region, $\mathbf{J}$ is the electric current density, dS_1 and dS_2 are the differential surfaces on the two antennas, and V and I are the voltages and currents at the ports of the antennas. Using transmission line theory, the voltages on the two antennas can be determined as a sum of self and mutual impedances and currents as in

$$V_1 = Z_{11} I_1 + Z_{12} I_2 \tag{4.10}$$

$$V_2 = Z_{21} I_1 + Z_{22} I_2 \tag{4.11}$$

where Z_{mn} is the impedance between antennas m and n. By then combining Equations 4.9, 4.10, and 4.11, the expression relating the self and mutual impedances and the power incident on each antenna can be derived as

$$\begin{aligned} &Z_{11}|I_1|^2 + Z_{12} I_1^* I_2 + Z_{21} I_1 I_2^* + Z_{22}|I_2|^2 = \\ &- \iint_{S_1} \mathbf{E}_{11} \mathbf{J}_1^* dS_1 - \iint_{S_1} \mathbf{E}_{12} \mathbf{J}_1^* dS_1 - \iint_{S_2} \mathbf{E}_{21} \mathbf{J}_2^* dS_2 - \iint_{S_2} \mathbf{E}_{22} \mathbf{J}_2^* dS_2. \end{aligned} \tag{4.12}$$

It can then be shown, by evaluating how the equation changes when different cur-

rents are removed, that the mutual impedance between two dipole can be determined by the expression

$$Z_{12} = \frac{-1}{I_1^* I_2} \iint_{S_1} \mathbf{E}_{12} \mathbf{J}_1^* dS_1. \tag{4.13}$$

where $\mathbf{E}_{12}$, the electric field at slot 1 due to slot 2 and $\mathbf{J}_1$ is the electric current density on slot 1. Similarly, for a slot antenna, the mutual admittance can be evaluated by

$$Y_{12} = \frac{-1}{V_1^* V_2} \iint_{S_1} \mathbf{H}_{12} \mathbf{M}_1^* dS_1. \tag{4.14}$$

where $\mathbf{H}_{12}$, the magnetic field at slot 1 due to slot 2 and $\mathbf{M}_1$ is the magnetic current density on slot 1.

According to Nauwelaers [31], finding the mutual impedance and admittance using the Reciprocity Theorem is the most exact answer because it relies on fewer assumptions than the Induced EMF method. However, it is limited in that it is only valid when all materials are reciprocal and when the currents are the product of a real function. The slot antennas discussed in Section 2.1 have voltages and currents that are products of complex functions, which can only be handled by the Induced EMF method.

4.3 Input Impedance

The input impedance of the array can be derived from the network matrix of the array. Because this is a Yagi-Uda style array, there is only a single driven element so the matrix needs to be reduced to only have one input. Reducing a matrix is accomplished by loading the other ports. In the case of a dipole array with impedance parameters, the arms are typically shorted together so the ports of the parasitic ele-

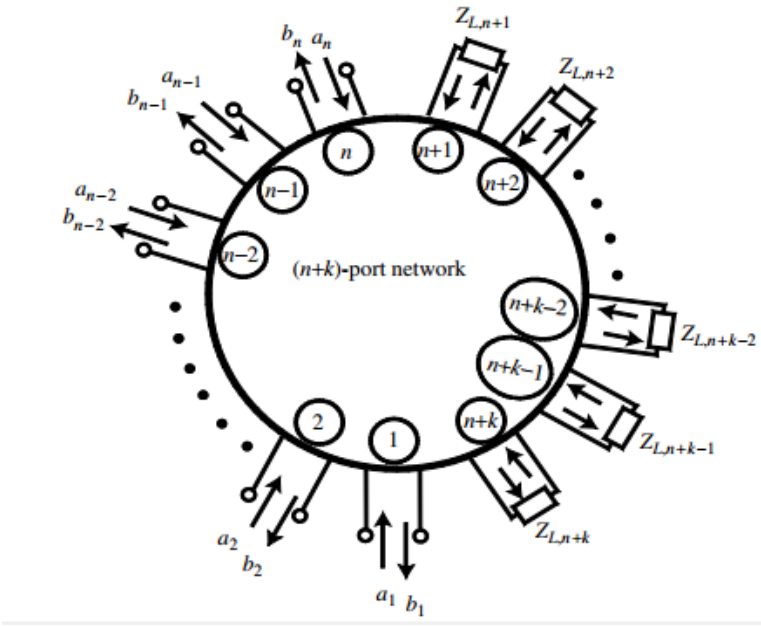

Figure 4.5: Multiport network reduced by loading k ports with load impedances [32].

ments are loaded with short circuits. For slot antennas with admittance parameters, the opposite sides of each parasitic slot are not connected so their ports are loaded with an open circuit. These matrices can then be reduced using a method from Chapter 2.2 of [32]. This method uses S-parameters to determine how the power reflects from the loaded ports and appears at the remaining ports. It first reconfigures the S-parameter matrix so that the last ports are the ones to be loaded with an impedance, then splits the matrix into four quadrants based on which ports are to be loaded. For example, Figure 4.5 shows an $n + k$ port network. The first n ports (ports 1 through n) remain unloaded while the last k ports (ports n through k) are to be loaded with impedances. So the S-parameter matrix of the system is split into

four quadrants as in

$$\left[\begin{array}{c} b_1 \\ b_2 \\ \vdots \\ b_n \\ \hline b_{n+1} \\ \vdots \\ b_{n+k} \end{array}\right] = \left[\begin{array}{cccc|ccc} S_{11} & S_{12} & \cdots & S_{1,n} & S_{1,n+1} & \cdots & S_{1,n+k} \\ S_{21} & S_{22} & \cdots & S_{2,n} & \vdots & \cdots & \vdots \\ \vdots & \vdots & \cdots & \vdots & \vdots & \cdots & \vdots \\ S_{n1} & S_{n2} & \cdots & S_{n,n} & S_{n,n+1} & \cdots & S_{n,n+k} \\ \hline S_{n+1,1} & \cdots & \cdots & S_{n+1,n} & S_{n+1,n+1} & \cdots & S_{n+1,n+k} \\ \vdots & \vdots & \cdots & \vdots & \vdots & \cdots & \vdots \\ S_{n+k,1} & \cdots & \cdots & S_{n+k,n} & S_{n+k,n+1} & \cdots & S_{n+k,n+k} \end{array}\right] \left[\begin{array}{c} a_1 \\ a_2 \\ \vdots \\ a_n \\ \hline a_{n+1} \\ \vdots \\ a_{n+k} \end{array}\right] \tag{4.15}$$

which can be written in shorthand as

$$\left[\begin{array}{c} \mathbf{B_1} \\ \hline \mathbf{B_2} \end{array}\right] = \left[\begin{array}{c|c} \mathbf{P_{11}} & \mathbf{P_{12}} \\ \hline \mathbf{P_{21}} & \mathbf{P_{22}} \end{array}\right] \left[\begin{array}{c} \mathbf{A_1} \\ \hline \mathbf{A_2} \end{array}\right]. \tag{4.16}$$

Next, a load matrix is defined as

$$\mathbf{\Gamma_L} = \begin{bmatrix} \Gamma_{L,n+1} & 0 & \cdots & 0 \\ 0 & \Gamma_{L,n+2} & \cdots & 0 \\ \vdots & \vdots & \ddots & \vdots \\ 0 & 0 & \cdots & \Gamma_{L,n+k} \end{bmatrix} \tag{4.17}$$

where $\Gamma_{L,i}$ is the reflection coefficient at port i due to the load impedance. Finally, the reduced n-port S-parameter matrix can be calculated as

$$\mathbf{S} = \mathbf{P_{11}} + (\mathbf{P_{12}\Gamma_L})(\mathbf{U_k} - \mathbf{P_{22}\Gamma_L})^{-1}\mathbf{P_{21}} \tag{4.18}$$

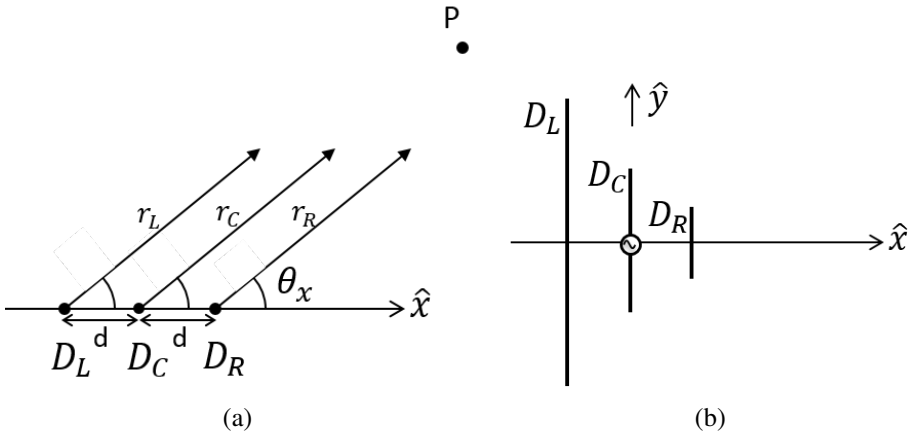

Figure 4.6: Yagi-Uda array of three linear dipoles spaced d apart along the x-axis. The x-z cut is shown in (a) and the x-y cut is shown in (b).

where $\mathbf{U_k}$ is an identity matrix of size k. If this method is used when all of the ports are loaded except for one, as is the case for a Yagi-Uda array, then the final S-parameter matrix is a single element composed of the reflection coefficient. The input impedance can then be found by

$$Z_{in} = Z_0 \left(\frac{1+S}{1-S} \right) \tag{4.19}$$

where Z_0 is the characteristic impedance of the remaining port and S is the only element in the reduced S-parameter matrix, also known as the reflection coefficient.

While the outer elements of a Yagi-Uda array will have some effect on the input impedance of the array as a whole, its effect is typically negligible at the operating frequency and can be approximated as simply the input impedance of the generator driven element.

4.4 Radiation Pattern

The radiation pattern of an antenna array can be derived from array factor. Array factor is a method to determine the radiation pattern of an array of similar linear elements using far-field approximations. For an array of three y-directed dipoles, shown in Figure 4.6, the electric field of the center element can be approximated as

$$E_C = I_C D_C \frac{e^{-jkr_C}}{4\pi r_C} \tag{4.20}$$

where k is the wave number, I_C is the current on the center dipole, D_C is the radiation pattern of the center dipole, and r_C is the distance from the center dipole to a far point, P. Using far-field approximations and assuming the patterns of the different dipoles, D_R and D_L are the similar to D_C, the electric field from the other dipoles can be described as

$$E_R = I_R D_R \frac{e^{-jkr_R}}{4\pi r_R} = I_R D_C \frac{e^{-jk(r_C - d\cos\theta_x)}}{4\pi r_C} = \frac{I_R}{I_C} E_C e^{jkd\cos\theta_x} \tag{4.21}$$

and

$$E_L = I_L D_L \frac{e^{-jkr_L}}{4\pi r_L} = I_L D_C \frac{e^{-jk(r_C + d\cos\theta_x)}}{4\pi r_C} = \frac{I_L}{I_C} E_C e^{-jkd\cos\theta_x} \tag{4.22}$$

where I_R and I_L are the currents on the right and left dipoles and the distances from the left and right dipoles to the point P, r_L and r_R can be approximated as

$$r_R = r_C - d\cos\theta_x \tag{4.23}$$

$$r_L = r_C + d\cos\theta_x. \tag{4.24}$$

The total field of the entire dipole array is then defined as

$$\begin{aligned} E_t &= E_L + E_C + E_R \\ &= \frac{I_L}{I_C} E_C e^{-jkd\cos\theta_x} + I_C \frac{e^{-jkr_C}}{4\pi r_C} + \frac{I_R}{I_C} E_C e^{jkd\cos\theta_x} \\ &= E_C \left(1 + \frac{I_L}{I_C} e^{-jkd\cos\theta_x} + \frac{I_R}{I_C} e^{jkd\cos\theta_x} \right) \\ &= E_C \times AF \end{aligned} \tag{4.25}$$

where AF is the Array Factor defined as

$$AF = \left(1 + \frac{I_L}{I_C} e^{-jkd\cos\theta_x} + \frac{I_R}{I_C} e^{jkd\cos\theta_x} \right) \tag{4.26}$$

for an array of dipoles [19]. Using this approximation, the total electric field can be calculated by multiplying the electric field of a single element by the array factor. Also, by plotting the array factor, it can be shown how the array is affecting the radiated fields and how the radiation is being directed.

It now becomes necessary to calculate the currents induced on the adjacent, parasitic dipoles as a result of the generator-driven dipole. As previously derived in Section 4.2, a network matrix of the linear array can be derived describing the relationships between each element. According to the impedance parameter definitions for the center dipole and the right dipole shown in Figure 4.4.a,

$$V_C = Z_{CC} I_C + Z_{CR} I_R \tag{4.27}$$

and

$$V_R = Z_{RC} I_C + Z_{RR} I_R = 0 \tag{4.28}$$

where the center dipole is the driven element and the right dipole is shorted. By

solving this system of equations separately for I_C and I_R, it can be found that

$$I_R = \frac{V_C Z_{RC}}{Z_{CR}Z_{RC} - Z_{CC}Z_{RR}} \tag{4.29}$$

and

$$I_C = \frac{-V_C Z_{RR}}{Z_{CR}Z_{RC} - Z_{CC}Z_{RR}} \tag{4.30}$$

so that

$$\frac{I_R}{I_C} = -\frac{Z_{RC}}{Z_{RR}}. \tag{4.31}$$

Now the equation for the total electric field of a dipole array can be solved as

$$\begin{aligned} E_t &= E_C \left(1 + \frac{I_L}{I_C} e^{-jkd\cos\theta_x} + \frac{I_R}{I_C} e^{jkd\cos\theta_x}\right) \\ &= E_C \left(1 - \frac{Z_{LC}}{Z_{LL}} e^{-jkd\cos\theta_x} - \frac{Z_{RC}}{Z_{RR}} e^{jkd\cos\theta_x}\right) \\ &= E_C \times AF. \end{aligned} \tag{4.32}$$

Similarly, the voltage relationships between the center and the right slot antennas can be shown to be

$$\frac{V_R}{V_C} = -\frac{Y_{RC}}{Y_{RR}}. \tag{4.33}$$

and the total electric field of a slot antenna is

$$\begin{aligned} E_t &= E_C \left(1 + \frac{V_L}{V_C} e^{-jkd\cos\theta_x} + \frac{V_R}{V_C} e^{jkd\cos\theta_x}\right) \\ &= E_C \left(1 - \frac{Y_{LC}}{Y_{LL}} e^{-jkd\cos\theta_x} - \frac{Y_{RC}}{Y_{RR}} e^{jkd\cos\theta_x}\right) \\ &= E_C \times AF. \end{aligned} \tag{4.34}$$

From the total electric field, the directivity and gain can be calculated. The radiation intensity, U, and directivity, D, shows the amount of power radiated in each

direction [19] is derived directly from the electric field as

$$\begin{aligned} U_{dipole} &= \frac{r_C^2}{2\eta}|E_t|^2 \\ &= \frac{I_C^2}{32\pi^2\eta}\left|D_C - \frac{Z_{LC}}{Z_{LL}}D_L e^{-jkd\cos\theta_x} - \frac{Z_{RC}}{Z_{RR}}D_R e^{jkd\cos\theta_x}\right|^2 \end{aligned} \tag{4.35}$$

for a dipole array and

$$U_{slot} = \frac{V_C^2}{32\pi^2\eta}\left|D_C - \frac{Y_{LC}}{Y_{LL}}D_L e^{-jkd\cos\theta_x} - \frac{Y_{RC}}{Y_{RR}}D_R e^{jkd\cos\theta_x}\right|^2 \tag{4.36}$$

for a slot array and the directivity is

$$D = \frac{4\pi U}{P_{rad}} \tag{4.37}$$

where P_{rad} is the power radiated and can be calculated by integrating the radiation intensity over an entire sphere:

$$P_{rad} = \iint_{\Omega} U d\Omega = \int_0^{2\pi}\int_0^{\pi} U\sin\theta d\theta d\phi. \tag{4.38}$$

Another important parameter to determine is the efficiency of the array. This will show how much power is lost due to parasitic losses and reflections between the transmission line and the antenna. Additionally, we will need to account for the aperture efficiency as the operating frequency changes. The total efficiency of the array can be calculated by

$$e_0 = e_r e_{cd} e_{ap} \tag{4.39}$$

where e_r is the reflection efficiency, e_{cd} is the conductor and dielectric efficiency, and e_{ap} is the aperture efficiency. The reflection efficiency determines how much

power reaches the antenna through the transmission line and can be calculated by

$$e_r = 1 - |\Gamma|^2 \tag{4.40}$$

where

$$\Gamma = \frac{Z_{in} - Z_0}{Z_{in} + Z_0}, \tag{4.41}$$

Z_{in} is the input impedance to the antenna, and Z_0 is the characteristic impedance of the feed line. The conductor and dielectric efficiency is the efficiency due to the losses in the surrounding media For a dipole antenna, it can be calculated by

$$e_{cd,dipole} = \frac{R_r}{R_L + R_r} \tag{4.42}$$

where R_r is the radiation resistance and R_L is the loss resistance. A typical half-wavelength dipole has a radiation resistance of 73 ohms and a loss resistance of

$$R_L = \frac{l}{4\pi a}\sqrt{\frac{\omega\mu_0}{2\sigma}} \tag{4.43}$$

where l is the length of the length of the dipole, a is the radius of the wire, ω is the radian frequency, μ_0 is the vacuum permeability, and σ is the conductivity of the wire. For a slot antenna, the conductor and dielectric efficiency is similar to that of a dipole, but uses conductance instead of resistance:

$$e_{cd,slot} = \frac{G_r}{G_L + G_r} \tag{4.44}$$

where G_r and G_L can either be per-unit-length parameters or take into account the entire antenna and can be calculated using the methods in Section 2.1. The aperture efficiency is a measure of how well the antenna radiates over frequency. In general,

the aperture efficiency can be calculated by

$$e_{ap} = \frac{A_{em}}{A_p} \tag{4.45}$$

where A_{em} is the maximum effective area of the antenna and A_p is the physical cross-sectional area of the antenna. The maximum effective area can be easily determined as

$$A_{em} = \frac{\lambda^2}{4\pi} D_{max}. \tag{4.46}$$

The realized gain of the antenna is then defined as

$$G = e_0 D. \tag{4.47}$$

The calculated array factor and radiation pattern of a Yagi-Uda dipole array for various array configurations are shown in Figure 4.7. It can be easily seen that as the left and right dipoles take on the roles of the reflector and director of a Yagi-Uda antenna, the array becomes more directive and pushes the radiation to one side. The array factor approximation and the HFSS simulation are in agreement in the main lobe and some of the back radiation is accounted for as well.

Similarly, the array factor and the radiation patterns of a Yagi-Uda slot array are shown in Figure 4.8. The array factor is very similar to that of the dipole array, which is expected. Additionally, the slot array radiation pattern with an infinite ground plane likewise resembles a dipole array pattern because there is no diffraction at the edges. This radiation pattern is also in agreement with HFSS in the main radiation lobe.

The radiation pattern of a slot array on a finite ground plane, shown in Figure 4.8.c is much different than the dipole array pattern. The diffraction due to

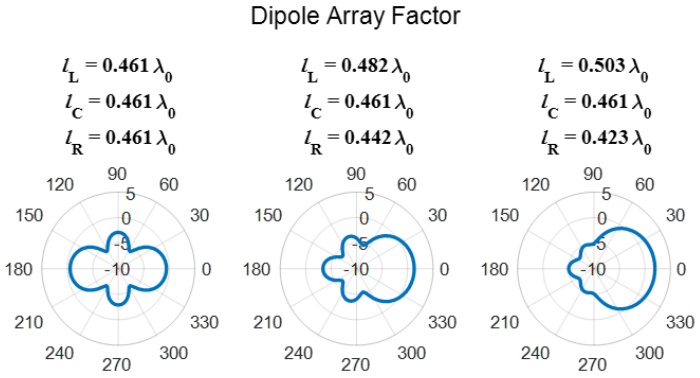

(a)

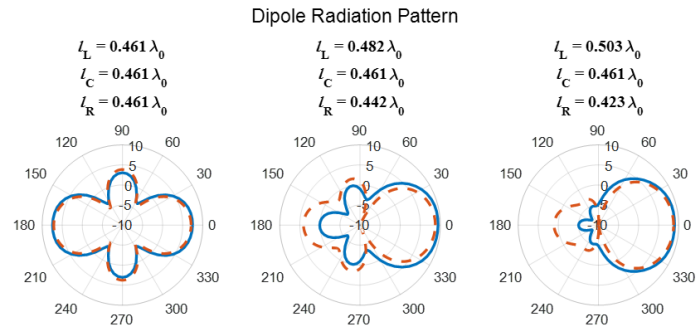

(b)

Figure 4.7: H-plane cut of the array factor and radiation pattern of a Yagi-Uda style dipole array. Directivity increases as the left and right dipoles become electrically larger and smaller than the fed element.

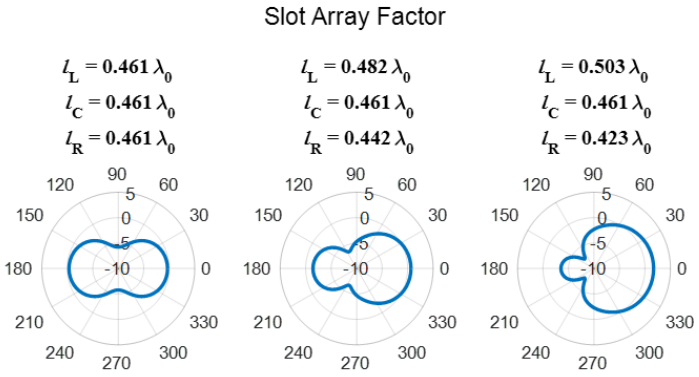

(a)

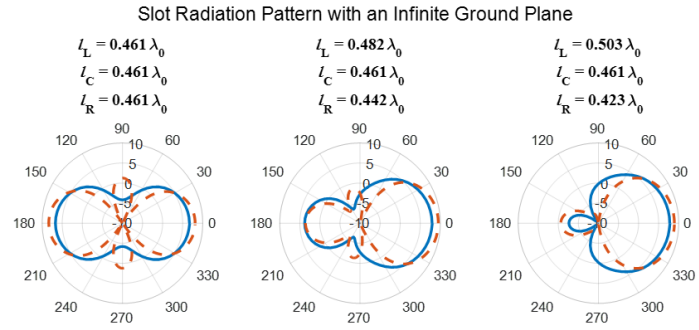

(b)

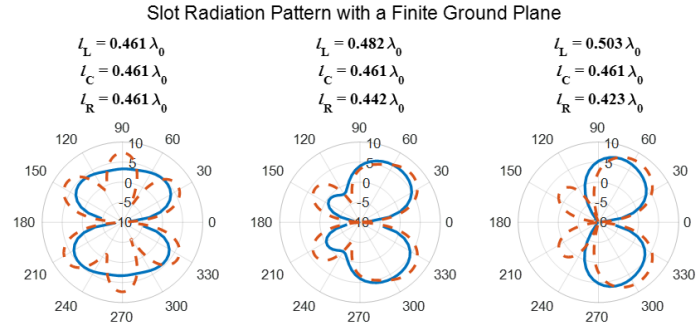

(c)

Figure 4.8: E-plane cut of the array factor and radiation pattern of a Yagi-Uda style slot array. Directivity increases as the left and right dipoles become electrically larger and smaller than the fed element.

the discontinuity of the ground plane edges perturbs the radiation pattern as previously discussed in Section 2.2.3. Additionally, the standard array factor model is no longer accurate as it assumes that the radiation pattern of each element on its own is identical to the center element, which is no longer true. A common solution to this problem is to take the average of the individual radiation patterns, but this method becomes more inaccurate as each element's radiation pattern becomes more dissimilar. A more accurate method would be to keep each radiation pattern separate while keeping the element current normalized to the center dipole so that the total electric field becomes

$$\begin{aligned} E_t &= E_L + E_C + E_R \\ &= I_L D_L \frac{e^{-jkr_C}}{4\pi r_C} e^{-jkd\cos\theta_x} + I_C D_C \frac{e^{-jkr_C}}{4\pi r_C} + I_R D_R \frac{e^{-jkr_C}}{4\pi r_C} e^{jkd\cos\theta_x} \\ &= I_C \frac{e^{-jkr_C}}{4\pi r_C} \left(D_C + \frac{I_L}{I_C} D_L e^{-jkd\cos\theta_x} + \frac{I_R}{I_C} D_R e^{jkd\cos\theta_x} \right) \\ &= I_C \frac{e^{-jkr_C}}{4\pi r_C} \left(D_C - \frac{Z_{LC}}{Z_{LL}} D_L e^{-jkd\cos\theta_x} - \frac{Z_{RC}}{Z_{RR}} D_R e^{jkd\cos\theta_x} \right). \end{aligned} \tag{4.48}$$

This method is compared to the array factor approximation and HFSS simulation results in Figure 4.9. The new electric field derivation in Equation 4.48 is more accurate than the previous array factor approximation and is in fairly good agreement with HFSS in the main lobe.

While it has been shown that different radiation patterns are possible using various configurations of Yagi-Uda slot antennas, It has not yet been shown that a pattern reconfigurable antenna is possible since the physical sizes of the antennas cannot be changed once they have been fabricated. Pattern reconfiguration can be achieved, however, by implementing reconfigurable end loads on the slot antennas. The end loads can be designed to reduce the size of the antenna while maintaining

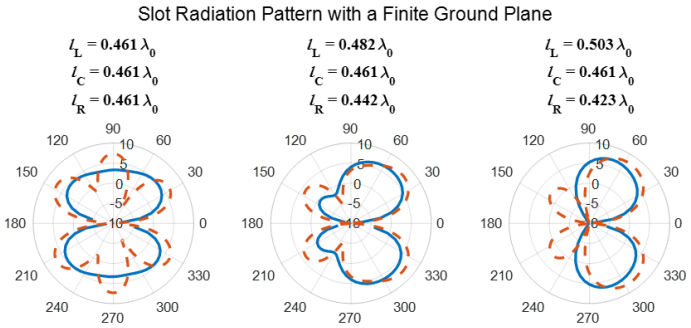

(a)

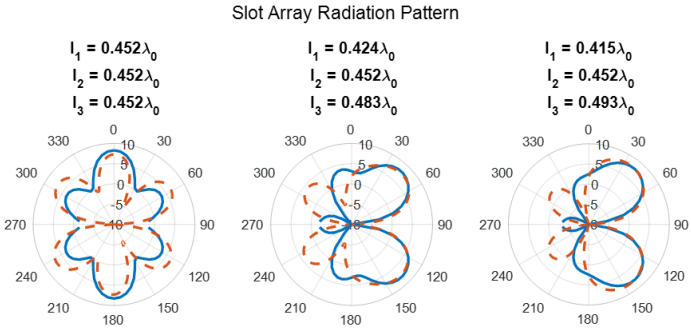

(b)

Figure 4.9: E-plane cut of the radiation pattern of a Yagi-Uda style slot array. (a) uses array factor assuming each element radiation pattern is the same, (b) takes the different radiation patterns into account.

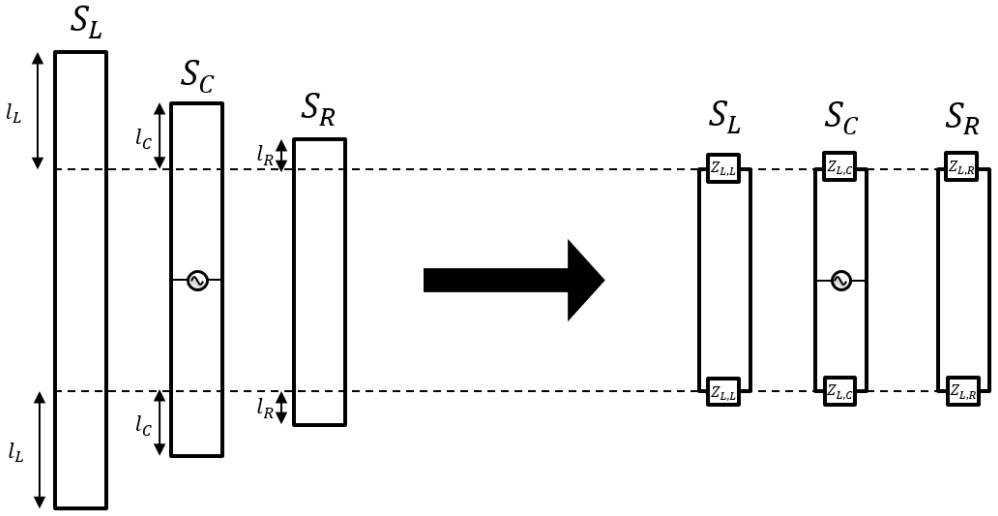

Figure 4.10: Linear Yagi-Uda slot antenna array truncated so that each element is the same electrical size. The end loads enable each to have a different effective size to maintain the directionality of the Yagi-Uda array.

the same operating frequency and a similar voltage distribution. By strategically adding end loads to a linear slot array, the elements can be truncated to be the same physical length while having different effective lengths, as shown in Figures 4.10 and 4.11. Then, as long as the end loads of the slots are reconfigurable, the effective lengths of the slots can be changed, redirecting the radiation in different directions. The appropriate end loads impedances can be calculated using transmission line theory

$$Z_{L,n} = jZ_0 \tan(\beta l_n) \tag{4.49}$$

$$L_n = \frac{Z_{L,n}}{j\omega} = \frac{Z_0}{\omega} \tan(\beta l_n) \tag{4.50}$$

where Z_0 is the characteristic impedance of the slotline, β is the propagation constant on the slotline, l_n is the length of truncated line for slot n, and $Z_{L,n}$ and L_n are the end load impedance and equivalent inductance needed to extend the effective length of the truncated slot to the correct effective length.

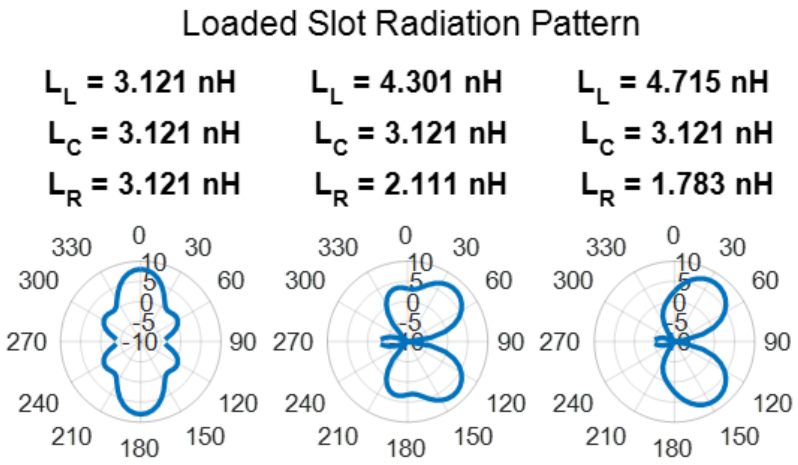

Figure 4.11: Radiation patterns of a slot antenna array loaded with ideal inductors to create an effective Yagi-Uda array. Each slot element is physically the same size, but the loads give each element an effective electrical length that can direct the radiation pattern like a Yagi-Uda antenna.

4.5 Conclusions

It has been shown previously and in this chapter that directionality can be achieved in a linear, Yagi-Uda style array and that the radiation pattern can be calculated using array factor and mutual coupling. While a transmission line coupling model is effective for adjacent transmission lines, it was determined that it did not take into account the far field radiation of the antenna and the Induced EMF method was used instead as it could easily determine the mutual admittance between two aperture fields. The mutual admittance was then used with the input admittances of the individual array elements to create a network matrix, from which was determined the input impedance to the array. Also from the mutual admittance, the total radiated fields and directivity of the array was derived by applying array factor and modifying it so that the individual radiation patterns of the elements could be used. Pattern reconfigurability was then achieved by truncated the slot array using

strategic end loads. By then simply changing the effective lengths of the elements in the array by tuning the end loads, the array could become more or less directive, changing the radiation pattern. In the next chapter, the RRELSA, which can effectively change its electrical length, will be used as an element to create a pattern reconfigurable array.

Chapter 5

RRELSA Array

In the previous chapters, it was shown that for a slot antenna, both the input impedance and the voltage distribution along the slot could be obtained using transmission line theory. Additionally it was shown that by strategically loading the ends of the slot, the antenna could be made to resonate at different frequencies than its physical structure would normally allow, and that by further tuning the load impedance the resonant frequency could be changed. Furthermore, methods were developed in Chapter 4 that enabled prediction of the input impedance and the radiation pattern of an array of linear elements, such as a slot antenna. By combining these methods with the RRELSA, a frequency reconfigurable slot antenna previously discussed in Chapter 3, it is possible to create a Yagi-Uda style array, shown in Figure 5.1, that is reconfigurable in both frequency and radiation pattern.

5.1 Basic Design

As established in Chapter 4, a Yagi-Uda array uses passive antennas of different lengths to achieve directivity. Furthermore, it was shown that the elements did not need to be physically different lengths as long the elements had similar effective length to those in a Yagi-Uda array. This can be achieved by strategically end

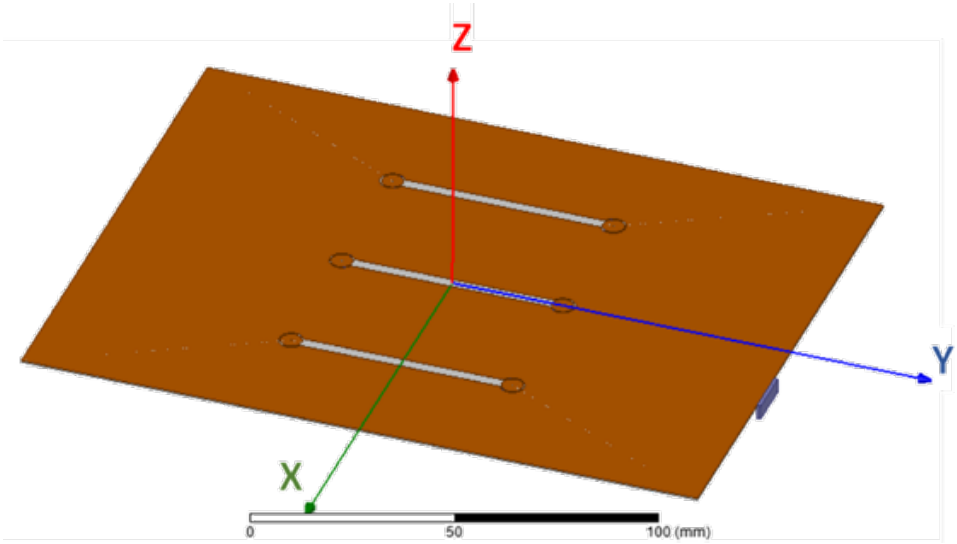

Figure 5.1: Design of the RRELSA Array. Three elements are placed next to each other in a Yagi-Uda configuration to achieve directionality. By tuning the outer elements, the radiation pattern can be bent from broadside.

loading the different elements. By then replacing the elements in a typical dipole Yagi-Uda array with an antenna that can change its effective length, such as the RRELSA from Chapter 3, a pattern reconfigurable array can be formed. Additionally, if the generator driven element is also frequency reconfigurable, the array is then frequency reconfigurable as well. However, the need to operate over a wide range of frequencies dictates that specifying physical dimensions as a function of a single wavelength is not sufficient, but that the array needs to be designed over a frequency range. For that reason, a brief study was conducted through HFSS to determine the optimal parameters of the array across frequency, as defined in Figure 5.2.

5.1.1 Element Tuning

As previously discussed, the initial design of the array was modeled after the Yagi-Uda dipole array using the design table shown in Figure 4.2. This table describes

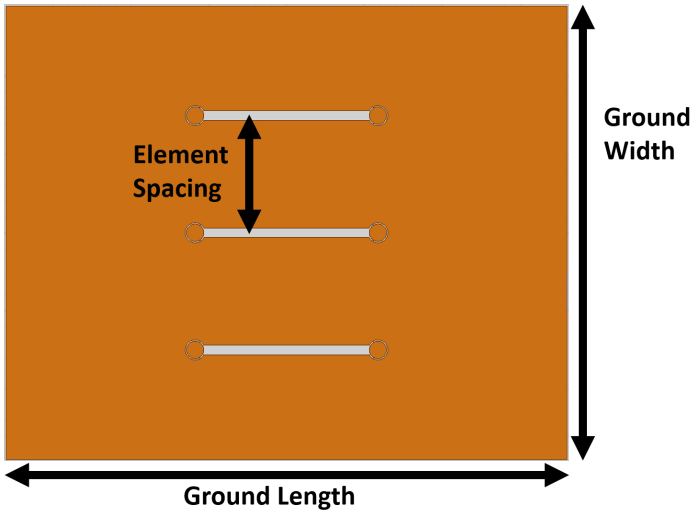

Figure 5.2: Definitions of three dimensions of the RRELSA array discussed in this chapter. The element spacing is defined from the center of each element, and the ground width and length are different dimensions of the ground plane.

what electrical lengths to use for each element in the array for different array sizes. A three element design was implemented so that it would be symmetric as the outer parasitic elements changed roles as reflector or director. In implementing the three element design, the approximate element lengths of the three elements can be obtained. However, the RRELSA does not easily lend itself to be defined in terms of electrical length. The table can still be used with the approximation that a dipole resonates at about 0.475λ and extrapolating the resonant frequency of the reflector, f_r, as it relates to the resonant frequency of the generator driven element, f_f, as in

$$0.482\lambda_f = 0.475\lambda_r \tag{5.1}$$

$$\frac{\lambda_f}{\lambda_r} = 0.985 = \frac{f_r}{f_f} \tag{5.2}$$

$$f_r = 0.985 f_f \tag{5.3}$$

where λ_f and λ_r is the wavelength at which the generator driven element and the reflector resonates respectively. Similarly, the resonant frequency of the director, f_d, can be determined by

$$0.442\lambda_f = 0.475\lambda_d \tag{5.4}$$

$$\frac{\lambda_f}{\lambda_d} = 1.075 = \frac{f_d}{f_f} \tag{5.5}$$

$$f_d = 1.075 f_f \tag{5.6}$$

where λ_d is the wavelength at which the director resonates. From these calculations, it is shown that the resonant frequency of the director should be $1.075 f_0$ and the resonant frequency of the reflector should be $0.985 f_0$. While this configuration served as a starting point to achieve directionality, if the reflector and director are tuned further from the driven element, the array becomes more directive. Once the impedance is found as a function of load capacitance for each element, it can be determined how to tune each element so that it resonates at the needed frequency to direct the radiation pattern.

5.1.2 Spacing

In determining different parameters of the array, the effects on radiation pattern, gain, and the size of the array need to taken into account. As stated previously, the Yagi-Uda design table suggests that the elements in the array should be spaced by about 0.2λ. The results from HFSS, shown in Figure 5.3.a and 5.3.b, primarily agree with this approximation, but additionally displays the effects as frequency changes. As the operating frequency decreases, there is a sharp decrease in the gain of the array, while there is a more gradual decrease as frequency increases. For this reason, the spacing between elements was increased to 0.25λ for the center

frequency of the array to allow the array to tune to a lower frequency. Because the spacing between the elements has such a large effect on the array, it is one of the limiting factors in designing a reconfigurable Yagi-Uda antenna. But if a different method of controlling the coupling were discovered, this limitation would be removed.

5.1.3 Ground Plane

A similar analysis was performed to determine the optimal dimensions of the ground plane, shown in Figures 5.3.c through 5.3.f. The total length of the ground plane does not have a large effect on the gain or radiation pattern, since it sits in a natural null of the slot antenna, due to the voltage distribution across each slot, as shown in Section 2.2. The length should still be large enough to accommodate the bias lines and the feeding network. The width of the ground plane, on the other hand, has a large effect on both the gain and the radiation pattern of the array. While the antenna remains directive, the gain and the side lobe level changes. Based on the results from HFSS, it was determined that the ground plane should be 1.33λ wide at the center frequency to reduce the side lobe levels as the array tunes in frequency.

5.1.4 Bent Microstrip Feed

The feed implemented with the original RRELSA design is not realizable with the array. The original microstrip line, shown in Figure 5.4.a, runs along the underside of the substrate perpendicular to the slot and with the addition of the other two slot elements, the feed would run under one of the outer parasitic slots, making it an another driven element. Therefore, a different feeding network needed to be designed. The new feed in Figure 5.4.b implements a gradual bend an eighth of a

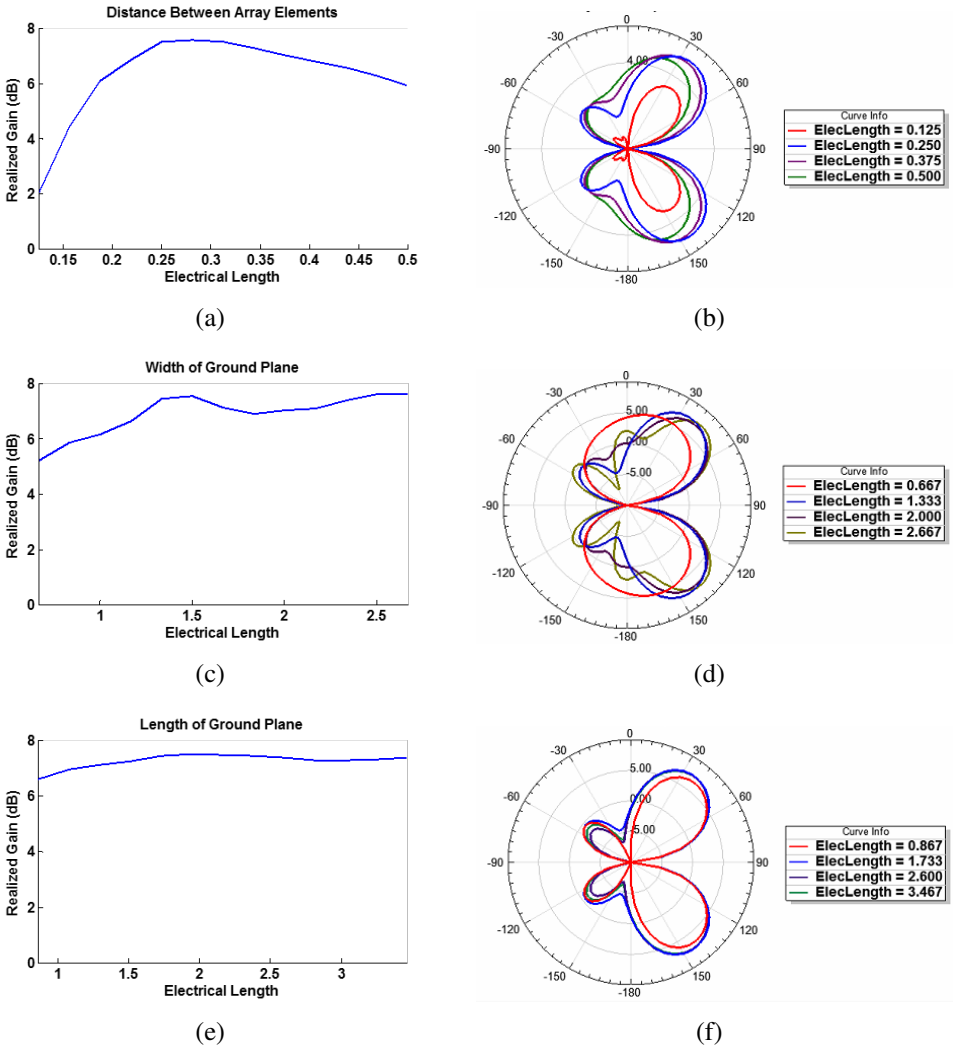

Figure 5.3: Analysis on the electrical size of the ground plane. The design was initialized with an element spacing of 37.5 mm, a ground width of 1.5λ, and a ground length of 2.0λ. Each dimensions was then varied individually from this design.

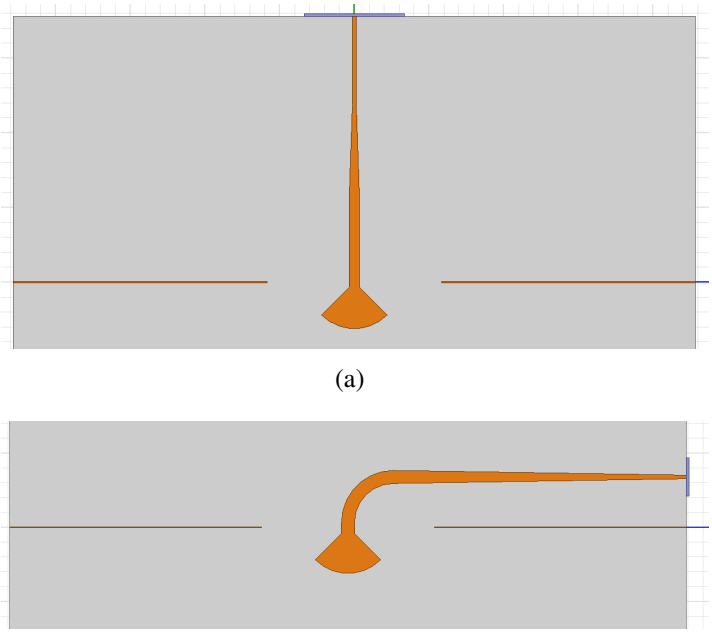

(a)

(b)

Figure 5.4: Tapered slot with a (a) straight feed as implemented in the original RRELSA design [2], and (b) a bent feed and radial tuning stub to be implemented in the array. Also shown are the bias lines that connect to the ring resonator loads.

wavelength past the center slot and runs directly in between the two slots. The bend has a turn with an inner radius of three times the width of the line so that there are minimal reflections due to the bend [15].

In addition to the bend in the microstrip feed line, the line also needs to be matched to the port impedance, which is typically 50Ω. Because the impedance of the microstrip under the slot must be tuned to couple with the slot antenna, shown in Section 3.5, it is unlikely that it would be the same impedance as the port. In order to resolve this mismatch, the line can be tapered between the microstrip bend and the port until the microstrip matches the port impedance, shown in Figure 5.4.b.

5.2 Final Designs and Results

The final designs for the array were created on Rogers substrates by first drilling the necessary vias using a milling machine, then using electroplating and photolithography to create the desired copper structures on the substrate. Wires were then attached to the bias lines and connected to DC generators so that the voltages across the varactors could be measured and controlled. These bias lines were made to run along the edges of the ground plane to minimize the effects on the radiation pattern of the array. The varactors were then soldered onto the ring resonators to complete the array. A DC block was also used to prevent DC power from reaching the VNA of the test equipment.

5.2.1 Original Design

The initial design of the RRELSA array was made by taking three of the original RRESLAs and placing them 37.5 mm apart from their center, as shown in Figure 5.5. They were placed on Rogers RO3003™, which is the same substrate used for the original RRELSA [2]. The ground plane was 145 by 180 mm to optimize the radiation pattern at 2 GHz and to accommodate the feeding network and bias lines. Also as in the original RRELSA paper, a radial stub was used in the feeding network to provide a broadband, low-impedance point on the microstrip line below the center slot [2].

Frequency Reconfiguration

When placed in an array, the RRELSA does not lose its ability to change its operating frequency. As previously discussed in Section 2.1.1, by tuning the center element the operating frequency of the entire array can be shifted, shown in Fig-

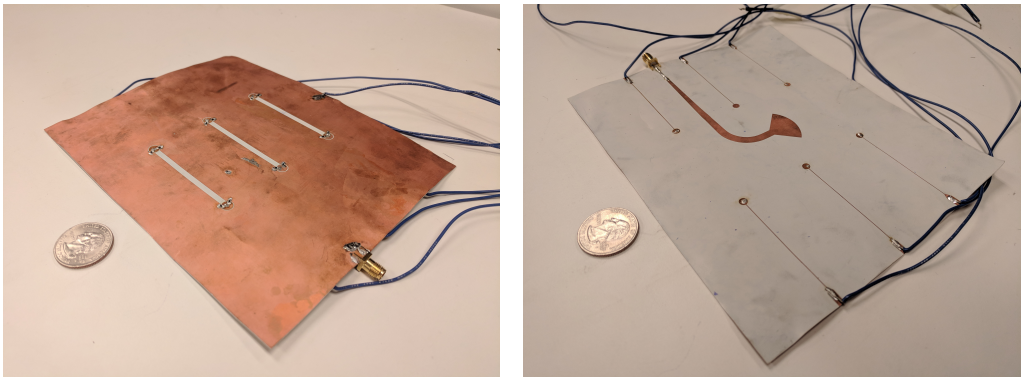

(a) (b)

Figure 5.5: Fabricated RRELSA array using the original design of the RRELSA from Szolc [2]. Bias lines can be seen along the edge of the ground plane to minimize their interference with the radiation pattern.

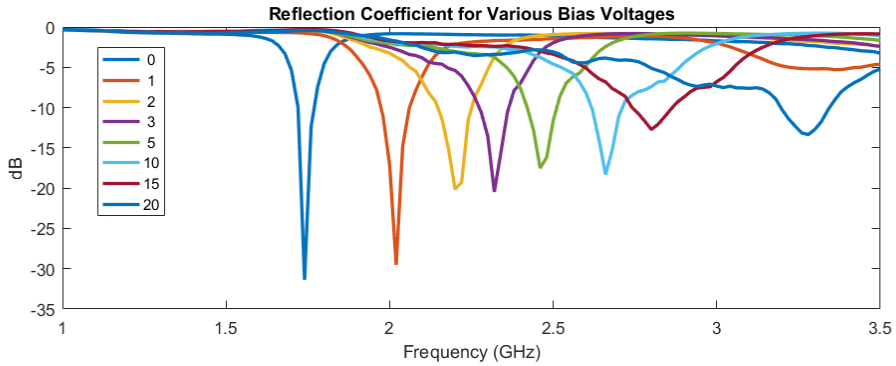

Figure 5.6: Measured reflection coefficient for the RRELSA array using the original design of the RRELSA in [2].

ure 5.6. As the biasing voltage is increased, the operating frequency shifts higher, but the impedance match diminishes. A reflection coefficient of less than -15 dB was achieved from 1.74 to 2.66 GHz with 0 to 10 volts using this configuration, obtaining a percent reconfigurable bandwidth of 42.7%.

Pattern Reconfiguration

While the RRELSA array can be frequency configured from 1.74 to 2.66 GHz, it is not possible to be pattern reconfigurable using all three elements for the entire

band. The nature of a Yagi-Uda antenna dictates that the parasitic elements resonate both above and below the operating frequency, preventing the driven element from tuning to those frequencies [6]. It is possible to achieve directivity using only two elements in order to increase the pattern reconfigurable bandwidth, but it would not be as directive. For this reason, 1.85 and 2.00 GHz were chosen to test the pattern reconfigurability of the array. The far-field radiation patterns for various pattern configuration were measured at those frequencies using an anechoic chamber and the results were compared to the circuit model derived previously in this thesis, shown in Figure 5.7 and 5.8.

While the circuit model does predict the operating frequency for the different biasing configurations, it does not accurately model the impedance match. This is most likely because the end loads are not modeled accurately in the original design of the RRELSA. The new design improves on this by implementing a taper with the ring resonator loads. The circuit model also accurately predicts the gain for the 2.0 GHz biasing and predicts the radiation pattern for the 1.85 and the 2.0 GHz biasings as well.

5.2.2 New Design at 2 GHz

In addition to the RRELSA array that used the antenna element from [2], another array was designed at 2 GHz that implements some of the improvements discussed in this thesis, shown in Figure 5.9. The substrate was changed to Rogers RT/duroid 5880™ to strengthen the substrate and make the array more robust. Because of this, the dielectric constant of the substrate changed form 3 to 2.2, requiring the width of each element to be increased to 4.6 mm. Additionally, the ring resonator end loads were changed to include a taper so that an accurate model of the load

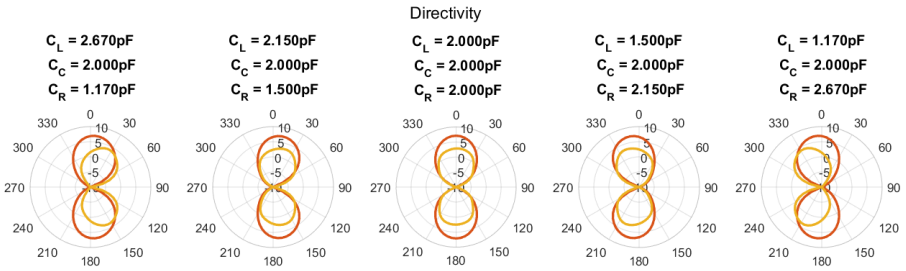

(a)

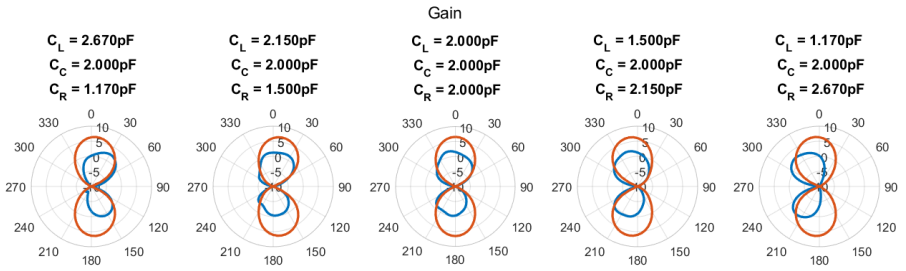

(b)

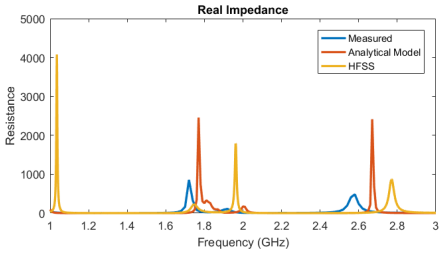

(c)

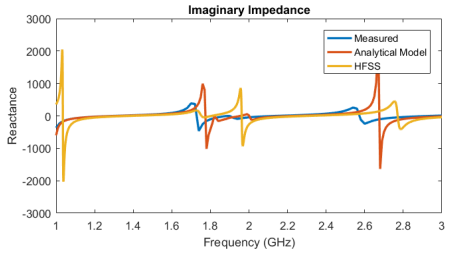

(d)

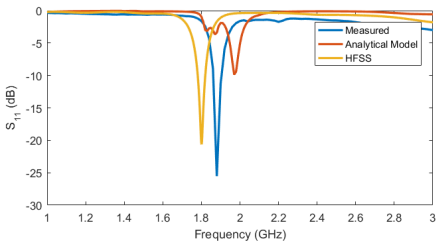

(e)

Figure 5.7: Directivity (a), realized gain (b), real (c) and imaginary (d) impedance, and the reflection coefficient (e) for the RRELSA array using the original element from [2] and tuned to 1.85 GHz. Measured values (blue) are compared to the circuit model described in this thesis (red) and an HFSS simulation (yellow).

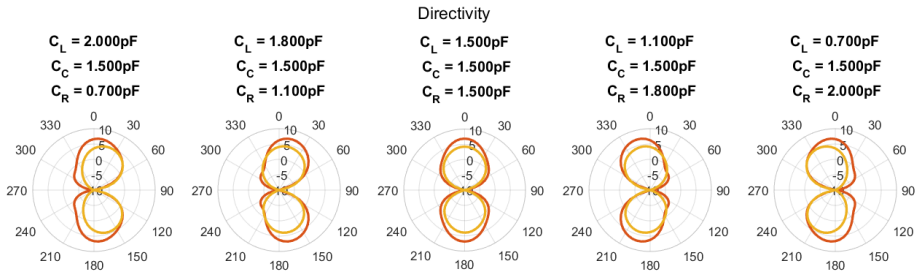

(a)

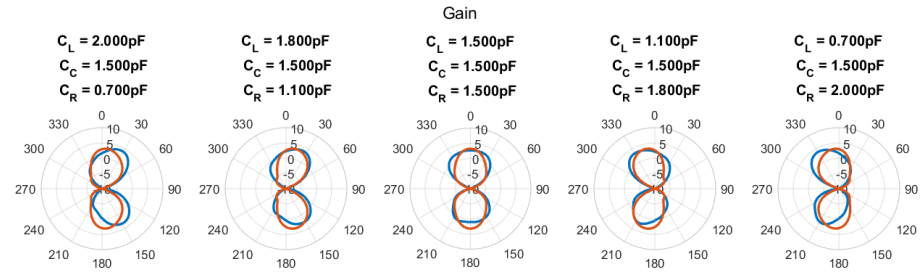

(b)

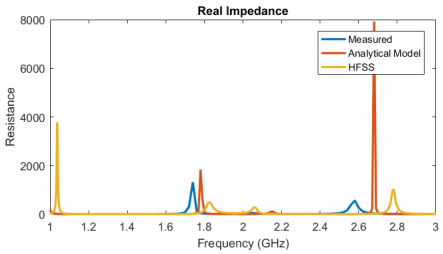

(c)

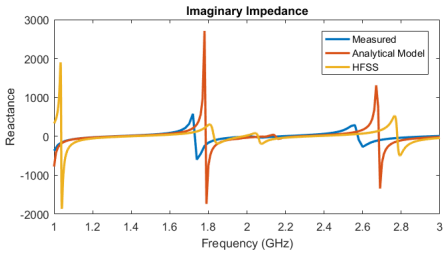

(d)

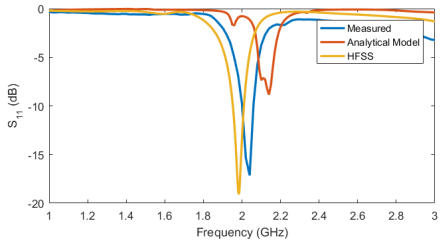

(e)

Figure 5.8: Directivity (a), realized gain (b), real (c) and imaginary (d) impedance, and the reflection coefficient (e) for the RRELSA array using the original element from [2] and tuned to 2.0 GHz. Measured values (blue) are compared to the circuit model described in this thesis (red) and an HFSS simulation (yellow).

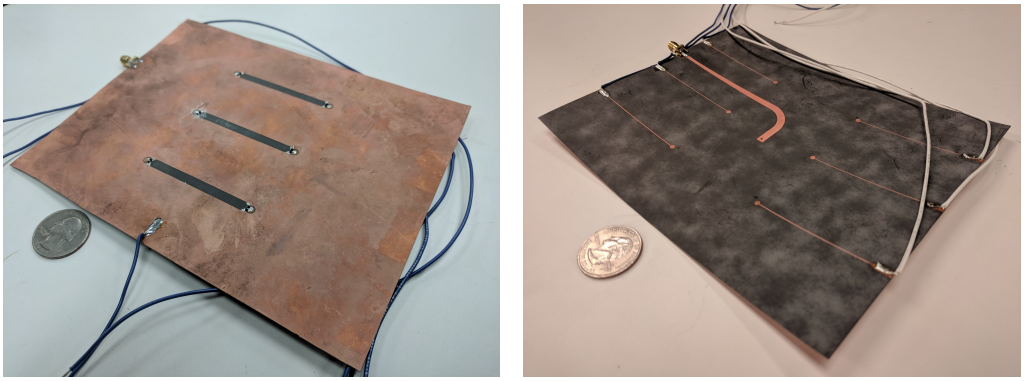

(a) (b)

Figure 5.9: Fabricated RRELSA array using a new design of the RRELSA. The new design primarily differs from the original by the tapered loads (a), and the microstrip feed line that is connected to the ground plane with a via (b).

could be used and different varactors were implemented that had a larger junction capacitance range. The ring resonators were also reduced in size to have a radius of 1.8 mm in order to increase the tunable range. Finally, the microstrip feed line was shorted to the ground plane with a via instead of using a radial stub to provide a more broadband low impedance point underneath the center slot antenna.

Frequency Reconfiguration

With the new design, the impedance match was improved in the higher frequencies, allowing the array to tune up to 3.16 GHz with a biasing voltage of 16 volts. The impedance match is reduced at the lower frequencies, but is still able to maintain a low reflection coefficient of -15 dB at 1.84 GHz using a voltage of 1 volt, and achieving a percent reconfigurable range of 54.7%.

Pattern Reconfiguration

As mentioned previously, the RRELSA array cannot be fully pattern reconfigurable over the entire band that it is frequency reconfigurable, but because the new design

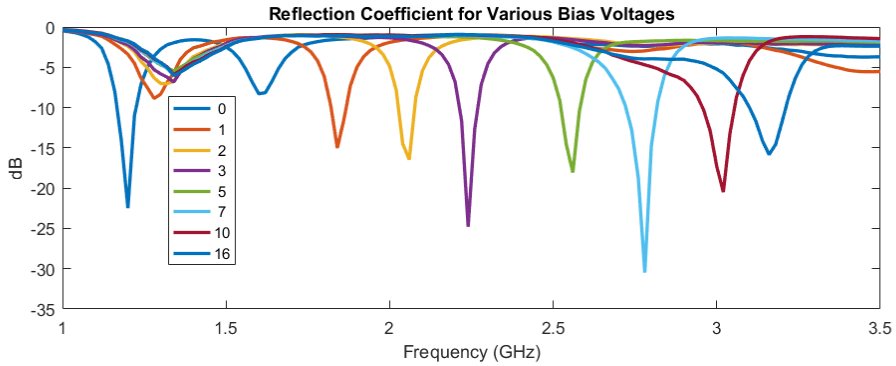

Figure 5.10: Measured reflection coefficient for the RRELSA array using a new design, as described in this thesis.

is matched in the higher frequencies, this array can be tuned to 2.3 GHz while maintaining full pattern reconfigurability. The radiation pattern of 2.3 GHz, as well as 2.0 GHz, was measured in the anechoic chamber and compared to the circuit model, shown in Figures 5.11 and 5.12.

With the new design, the circuit model can more accurately predict the operating frequency and the impedance match. Additionally, it can predict the radiation pattern of the 2.3 and 2.0 GHz biasings with agreement to measurements in the main lobes. The overall gain of the antenna matches well between the analytical model and measurements, though some losses may be unaccounted for due to the solder used in fabrication errors.

5.2.3 New Design at 4 GHz

In addition to the 2 GHz design, another array was designed for 4 GHz to illustrate that this work can be applied to a different center frequency. This array was much smaller, with a ground plane size of 90 by 72.5 mm, shown in Figure 5.13. Similarly, the rest of the array was also scaled down with respect to wavelength, including the ring resonators, which had a radius of 0.8 mm. Despite its small size,

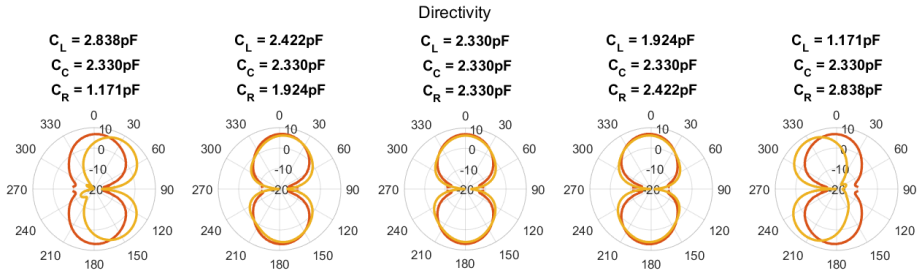

(a)

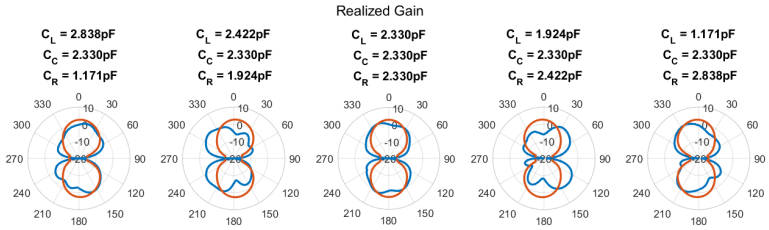

(b)

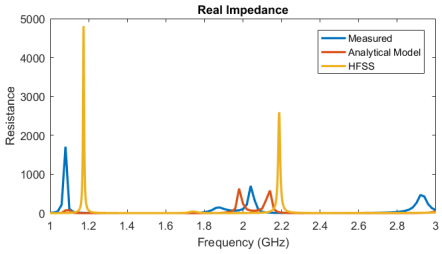

(c)

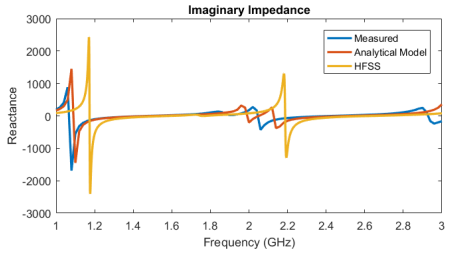

(d)

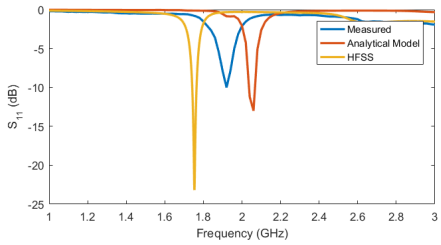

(e)

Figure 5.11: Directivity (a), realized gain (b), real (c) and imaginary (d) impedance, and the reflection coefficient (e) for the redesigned RRELSA array centered and tuned to 2.0 GHz. Measured values (blue) are compared to the circuit model described in this thesis (red) and an HFSS simulation (yellow).

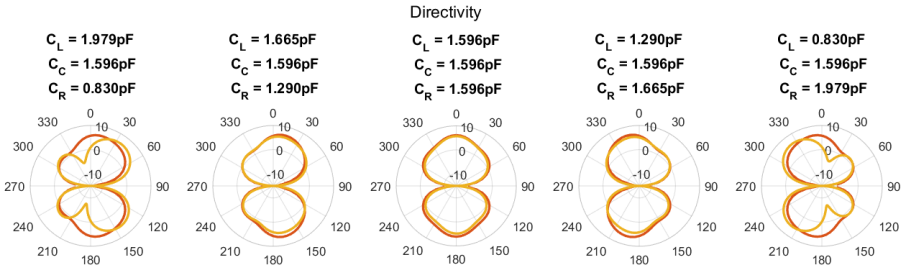

(a)

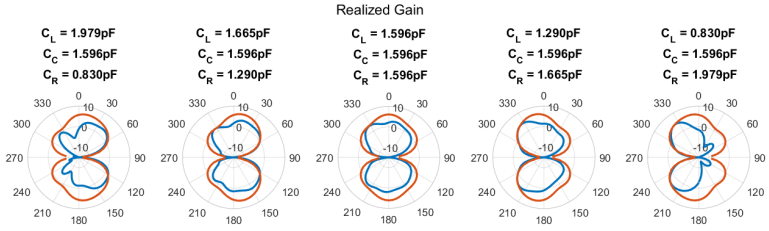

(b)

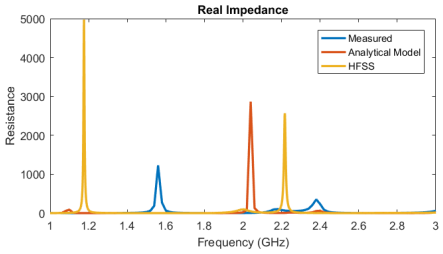

(c)

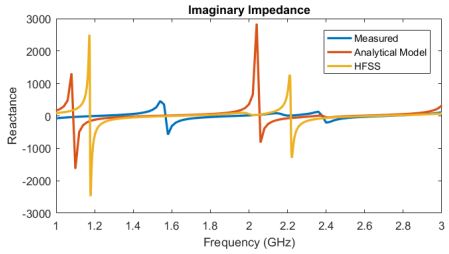

(d)

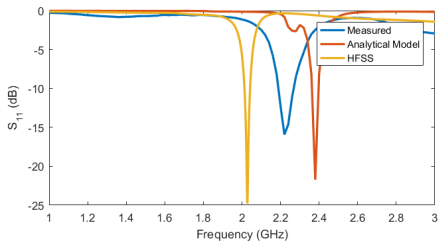

(e)

Figure 5.12: Directivity (a), realized gain (b), real (c) and imaginary (d) impedance, and the reflection coefficient (e) for the redesigned RRELSA array centered at 2 GHz and tuned to 2.3 GHz. Measured values (blue) are compared to the circuit model described in this thesis (red) and an HFSS simulation (yellow).

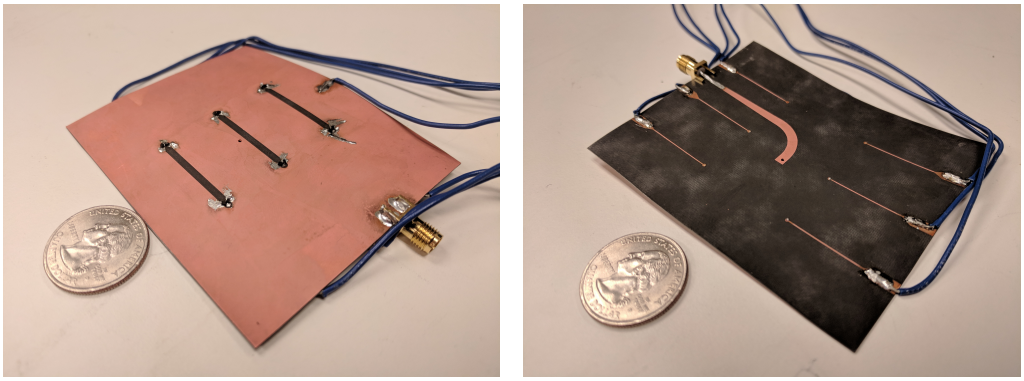

(a) (b)

Figure 5.13: Fabricated RRELSA array using a new design of the RRELSA. This array has about a quarter the surface area of the other designs.

this design was able to be fabricated and the measurements and simulations are compared in Figures 5.15 and 5.16. This design approaches the upper limit of reasonable frequency ranges to design for without a significant change in the design of the array. Future work will include modifying the array to make the fabrication more reliable at even higher frequencies.

Frequency Reconfiguration

At the design frequency of 4 GHz, the array is impedance matched for a biasing voltage of 10 V. However, as the array tunes to lower frequencies, the match deteriorates. The array is still able to achieve a match from 2.58 to 4.24 GHz, with a percent reconfigurable bandwidth of 50.3%.

Pattern Reconfiguration

Similar to the previous designs, the RRELSA array cannot be fully pattern reconfigurable over its entire reconfigurable bandwidth. Because this design can be recongfigured between 2.58 and 4.24 GHz, the radiation patterns of the array for

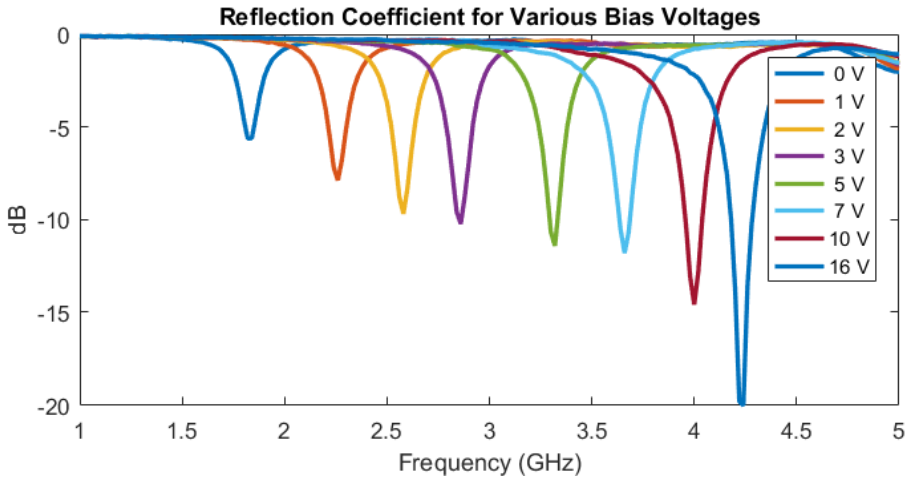

Figure 5.14: Measured reflection coefficient for the RRELSA array using the new array and designed at 4 GHz.

various biasing configurations were measured at 3.0 and 4.0 GHz. This leaved enough bandwidth on either side of these frequencies to achieve a Yagi-Uda configuration. The measurements of the array at these frequencies is compared to the circuit model, shown in Figures 5.15 and 5.16.

While the circuit model matches will with the HFSS simulations, the measurements are significantly reduced in gain. This is most likely due to error in the physically realized ring resonators. The radius of the ring resonators were so small, that there was not enough space for both of them to be placed accurately. This likely reduced the radiation efficiency of the array. Despite this, the array can still be reconfigured at 4 GHz, achieving a maximum beam tilt of about 30 degrees from broadside. At 3 GHz, the array displays a very little pattern reconfiguration, only steering the beam 1 degree. Most likely, this is because of the relatively poorer impedance match shown in Figure 5.14 at this frequency, combined with the low gain of the array, which reduced the coupling between the different elements.

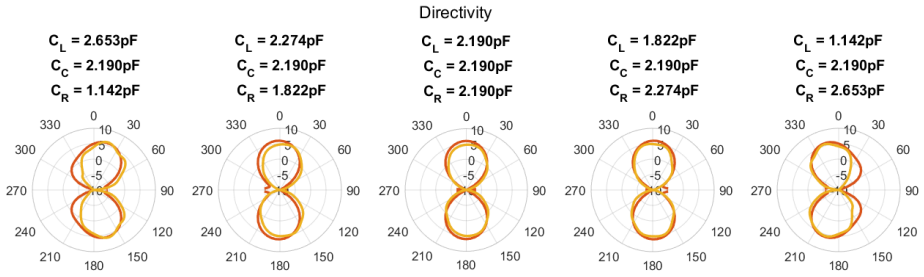

(a)

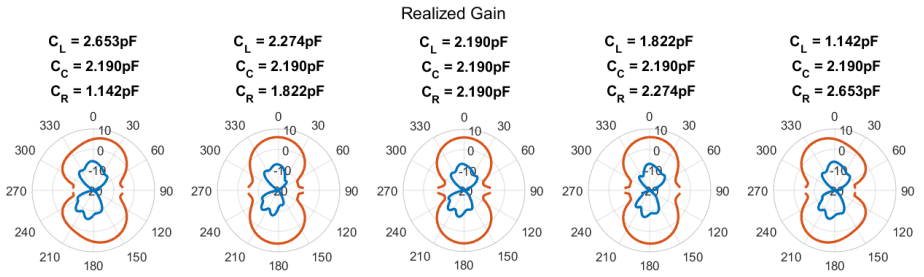

(b)

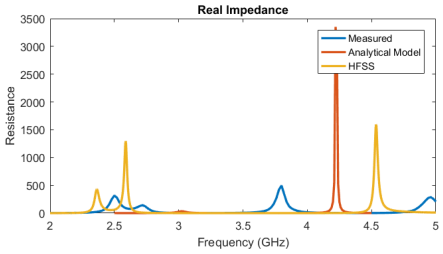

(c)

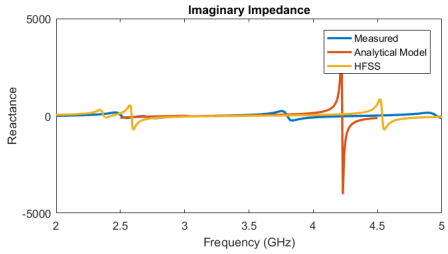

(d)

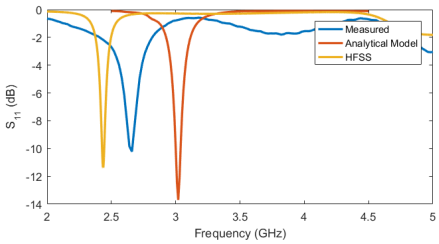

(e)

Figure 5.15: Directivity (a), realized gain (b), real (c) and imaginary (d) impedance, and the reflection coefficient (e) for the redesigned RRELSA array centered at 4 GHz and tuned to 3 GHz. Measured values (blue) are compared to the circuit model described in this thesis (red) and an HFSS simulation (yellow).

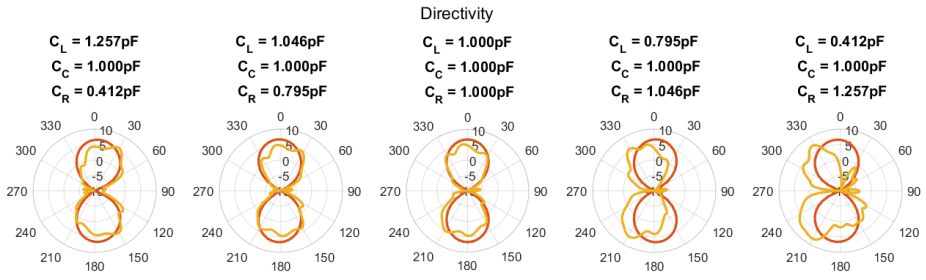

(a)

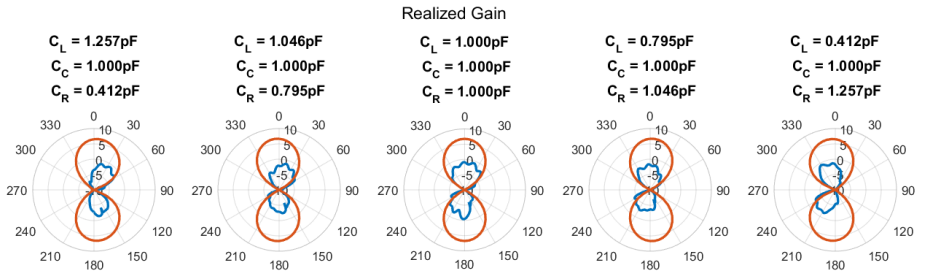

(b)

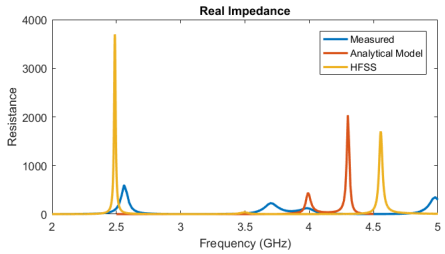

(c)

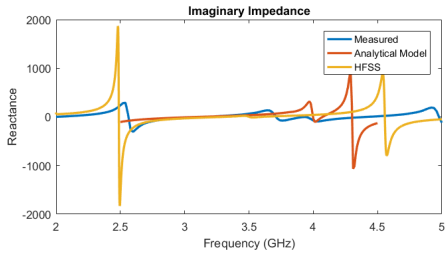

(d)

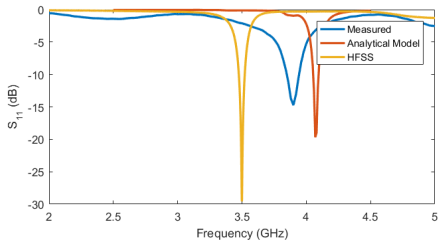

(e)

Figure 5.16: Directivity (a), realized gain (b), real (c) and imaginary (d) impedance, and the reflection coefficient (e) for the redesigned RRELSA array centered and tuned to 4 GHz. Measured values (blue) are compared to the circuit model described in this thesis (red) and an HFSS simulation (yellow).

Table 5.1: Tabulated measurement results from the three designs, specifically gain, percent reconfigurable bandwidth, and the maximum beam tilt achieved for each design. A range of measured gain is given because the arrays are pattern reconfigurable and it can change based on the configuration.

Design	Gain (dBi)	Reconfigurable Bandwidth	Max Beam Tilt
Original Array	1.91 - 3.78	42.7 %	34°
2.0 GHz Array	1.3 - 3.05	54.7 %	30°
4.0 GHz Array	-7.15 - -0.5	50.2 %	32°

5.3 Conclusions

This chapter finished the basic design of the RRELSA array. Three frequency reconfigurable elements were combined to create a frequency and pattern reconfigurable array modeled after the Yagi-Uda antenna. Although there is not an easily apparent way to determine the effective length of each element, an approximation can be made using the resonant frequencies of the elements to tune them to the desired configuration. The spacing between the elements was analyzed and discovered to be one of the limiting factors in the array. Future work could develop a different coupling mechanism that could be reconfigured to mitigate this problem. The effects of ground plane size was also discussed and a bent microstrip feed was designed to feed only the center element with minimal reflections on the line. Finally, three designs for the RRELSA array were introduced: a design that had the original RRESLA elements from [2] and two modified designs centered at 2 GHz and 4 GHz. Table 5.1 enumerates several of the mores significant characteristics of each design. The circuit model developed in previous chapters was shown to accurately predict many of the artifacts in the radiation pattern and impedance match of the different arrays, though it could be improved in future work.

Chapter 6

Conclusions and Future Work

6.1 Conclusions

Versatile antennas enable the system to operate in a crowded spectrum or noisy environment. A system that can employ both frequency and pattern reconfiguration can easily switch to an unused frequency and direct itself at a target or away from a noisy source to improve the quality of its transmission and reception. This work shows a method to designing an antenna that is continuously reconfigurable in both frequency and pattern. Antenna reconfiguration is conventionally achieved by implementing switches or moving parts to change the impedance or effective size of the antenna, but a system that instead is configured electronically would be more reliable over time. The method described here implements a Yagi-Uda style array made up of frequency reconfigurable elements, in particular the Ring Resonator End Loaded Slot Antenna [2]. This method uses standard transmission line and array theory to design the array and determine its electrical properties, such as the input impedance and radiation pattern. There are several advantages to using this method such as the ability to continuously tune across frequency, in addition to continuous pattern reconfiguration, instead of having a few set modes for the system. The circuit model enables an initial design of the system without using a full wave

computational solver. The reconfigurable ring resonator end loads use varactors, which have a negligible power draw. Its planar design and the single driven element makes the antenna simple to fabricate and implement into an existing system. This model is a powerful tool that enables simultaneous frequency and radiation pattern reconfiguration in a simple design.

6.2 Scientific Impact

The model described in this work can impact the scientific community in several key ways. To the best of the author's knowledge, this is the first antenna with the ability to simultaneously and continuously reconfigure in both frequency and pattern. The circuit model also developed here will provide the groundwork for further research into similar antennas, allowing more complex designs to be accurately modeled. Additionally, while the ring resonator end loads enable the slot antenna to be reconfigurable, the model is not limited to using them. The circuit model can use any designed end load as long as the the input impedance of the load is known.

6.3 Future Work

Several different paths for future research exist for this model. Primarily, the coupling between the slot antenna elements is calculated using the voltage distribution across the slot. The model for the voltage distribution, derived in Section 2.1.2, is a modal analysis on the different waveforms that can exist on the slot antenna under a certain configuration. The weighting of the different modes is an approximation based on the relation between the modal propagation constants and the driven propagation constant on the slot antenna. This expression could be improved which would also improve the calculation of the coupling between antenna elements.

The design could also be made more robust and able to tolerate fabrication errors, allowing for smaller designs. By modifying the ring resonator end loads so that they could be physically larger, the margin for error in the fabrication process would increase and higher frequency designs could be created. The other parameters of the antenna, such as the length of the slot, would need to be changed as well to account for the shift in load impedance.

Future work also includes offset biasing by having different voltages on the end loads of the same element. This technique could account for a change in impedance of the media surrounding the antenna, such as when the antenna is set down or something is set on top of it that it was not initially designed for. Different loads could also be tested to provide a better impedance match or to improve the reconfigurable range of the antenna. Also, as mentioned in Section 5.1.2, if a method to control the coupling between the elements could be established, then the spacing between the elements would cease to become a limiting factor to the performance of the array. This work opens up several research topics that could be explored and would improve both the model presented here as well as future designs of dual reconfigurable antennas.

References

[1] Y. Tawk, M. Bkassiny, G. El-Howayek, S. K. Jayaweera, K. Avery, and C. G. Christodoulou, "Reconfigurable front-end antennas for cognitive radio applications", *IET microwaves, antennas & propagation*, vol. 5, no. 8, pp. 985–992, 2011.

[2] L. Szolc, T. Poydence, and J. Ruyle, "Frequency-agile ring resonator end-loaded slot antenna", *Microwave and Optical Technology Letters*, vol. 59, no. 8, pp. 1876–1882, 2017.

[3] J. T. Bernhard, "Reconfigurable antennas", *Synthesis lectures on antennas*, vol. 2, no. 1, pp. 1–66, 2007.

[4] W. H. V. Aulock, "Properties of phased arrays", *Proceedings of the IRE*, vol. 48, no. 10, pp. 1715–1727, Oct. 1960, ISSN: 0096-8390. DOI: 10.1109/JRPROC.1960.287523.

[5] R. J. Mailloux, *Phased array antenna handbook*. Artech House Boston, 2005, vol. 2.

[6] S. Uda and Y. Mushiake, *Yagi-uda antenna*. Research Institute of Electrical Communication, Tohoku University, 1954.

[7] S. Zhang, G. Huff, J. Feng, and J. Bernhard, "A pattern reconfigurable microstrip parasitic array", *IEEE Transactions on Antennas and Propagation*, vol. 52, no. 10, pp. 2773–2776, 2004.

[8] B. Ke, Y. Qian, and T. Itoh, "A two-element yagi-uda array using tunable slot antenna", in *Asia Pacific Microwave Conference, Hong Kong, China*, 1997, pp. 437–440.

[9] T. Limpiti and M. Krairiksh, "Design of a 24 ghz pattern reconfigurable slotted yagi-uda antenna on substrate integrated waveguide", in *Electrical Engineering/Electronics, Computer, Telecommunications and Information Tech-*

nology (ECTI-CON), 2013 10th International Conference on, IEEE, 2013, pp. 1–4.

[10] H. King, "Mutual impedance of unequal length antennas in echelon", *IRE Transactions on Antennas and Propagation*, vol. 5, no. 3, pp. 306–313, 1957.

[11] R. Mailloux, "Antenna and wave theories of infinite yagi-uda arrays", *IEEE Transactions on Antennas and Propagation*, vol. 13, no. 4, pp. 499–506, Jul. 1965, ISSN: 0018-926X. DOI: 10.1109/TAP.1965.1138470.

[12] J. Huang, "Planar microstrip yagi array antenna", in *Antennas and Propagation Society International Symposium, 1989. AP-S. Digest*, IEEE, 1989, pp. 894–897.

[13] J. Ruyle, "Small, dual band, placement insensitive antennas", PhD thesis, University of Illinois, 2011.

[14] M. Himdi and J. P. Daniel, "Analysis of printed linear slot antenna using lossy transmission line model", *Electronics Letters*, vol. 28, no. 6, pp. 598–601, Mar. 1992, ISSN: 0013-5194. DOI: 10.1049/el:19920377.

[15] D. Pozar, *Microwave engineering*. John Wiley & Sons, 2005.

[16] S. B. Cohn, "Slot line on a dielectric substrate", *IEEE Transactions on Microwave Theory and Techniques*, vol. 17, no. 10, pp. 768–778, Oct. 1969, ISSN: 0018-9480. DOI: 10.1109/TMTT.1969.1127058.

[17] C. A. Balanis, *Advanced engineering electromagnetics*, 2nd ed. John Wiley & Sons, 2012.

[18] D. K. Cheng, *Field and wave electromagnetics*, 2nd ed. Addison-Wesley, 1989.

[19] C. A. Balanis, *Antenna theory: Analysis and design*, 3rd ed. John Wiley & Sons, 2016.

[20] H. G. Booker, "Slot aerials and their relation to complementary wire aerials (babinet's principle)", *Journal of the Institution of Electrical Engineers-Part IIIA: Radiolocation*, vol. 93, no. 4, pp. 620–626, 1946.

[21] W. L. Stutzman and G. A. Thiele, *Antenna theory and design*, 2nd ed. John Wiley & Sons, 1998.

[22] M. K. Kim, K. Kim, Y. H. Suh, and I. Park, "A t-shaped microstrip-line-fed wide slot antenna", in *IEEE Antennas and Propagation Society International Symposium. Transmitting Waves of Progress to the Next Millennium. 2000 Digest. Held in conjunction with: USNC/URSI National Radio Science Meeting (C*, vol. 3, Jul. 2000, 1500–1503 vol.3. DOI: 10.1109/APS.2000.874491.

[23] Y. Yoshimura, "A microstripline slot antenna (short papers)", *IEEE Transactions on Microwave Theory and Techniques*, vol. 20, no. 11, pp. 760–762, Nov. 1972, ISSN: 0018-9480. DOI: 10.1109/TMTT.1972.1127868.

[24] M. Zinieris, R. Sloan, and L. Davis, "A broadband microstrip-to-slot-line transition", *Microwave and Optical technology letters*, vol. 18, no. 5, pp. 339–342, 1998.

[25] F. Giannini, R. Sorrentino, and J. Vrba, "Planar circuit analysis of microstrip radial stub (short paper)", *IEEE Transactions on Microwave Theory and Techniques*, vol. 32, no. 12, pp. 1652–1655, Dec. 1984, ISSN: 0018-9480. DOI: 10.1109/TMTT.1984.1132907.

[26] M. E. Goldfarb and R. A. Pucel, "Modeling via hole grounds in microstrip", *IEEE microwave and guided wave letters*, vol. 1, no. 6, pp. 135–137, 1991.

[27] A. Matland, "Improved vertical coupling between printed planar transmission lines", eng, Master's thesis, University of Oklahoma, 2016.

[28] J. B. Knorr, "Slot-line transitions (short papers)", *IEEE Transactions on Microwave Theory and Techniques*, vol. 22, no. 5, pp. 548–554, May 1974, ISSN: 0018-9480. DOI: 10.1109/TMTT.1974.1128278.

[29] E. Brenner and M. Javid, "Analysis of electric circuits", 1967.

[30] P. Winniford, "Analytical matrix method to analyze multiline transmission line structures", Master's thesis, University of Oklahoma, 2015.

[31] B. K. J. C. Nauwelaers and A. R. Van De Capelle, "Integrals for the mutual coupling between dipoles or between slots: With or without complex conjugate?", *IEEE Transactions on Antennas and Propagation*, vol. 36, no. 10, pp. 1375–1381, 1988.

[32] H.-R. Ahn, *Asymmetric passive components in microwave integrated circuits*. John Wiley & Sons, 2005.